Computers & Geosciences 206 (2026) 106023

Contents lists available at ScienceDirect

Computers and Geosciences

journal homepage: www.elsevier.com/locate/cageo

Research paper

Simulating major element diffusion in garnet using realistic 3D geometries

Hugo Dominguez [a,b,c,*], Nathan Mäder [a], Pierre Lanari [a,d]

[a] Institute of Geological Sciences, University of Bern, Bern 3012, Switzerland
[b] Institute of Geosciences, Johannes Gutenberg University, Mainz 55099, Germany
[c] Mainz Institute of Multiscale Modelling (M3ODEL), Mainz 55099, Germany
[d] Institute of Earth Sciences, University of Lausanne, Lausanne 1015, Switzerland

ARTICLE INFO

Dataset link: https://zenodo.org/records/15045718

Keywords:
Garnet
3D modelling
Chemical diffusion
Stabilised explicit methods
GPU
Micro-computed tomography
Metamorphism

ABSTRACT

Chemical diffusion of major elements in garnet is a common phenomenon in amphibolite to granulite facies metamorphic rocks. The study of this process has led to important constraints on the rate and timescale of metamorphism, for instance using geospeedometry and forward thermodynamic modelling. However, to date, most models have assumed spherical coordinates and simple geometries when modelling diffusion in garnet. In this study, we present a framework for running 3D multicomponent diffusion models from real grain geometries obtained by micro-computed tomography. We introduce an open-source code, DiffusionGarnet.jl, written for high performance in the Julia programming language. We demonstrate the high efficiency of the numerical solver, a stabilised explicit method, and its scalability using GPU acceleration. This approach is applied to two garnet grains with different characteristics, a euhedral well-shaped grain and a deformed sub-euhedral grain with a high connectivity to the matrix from core to rim. Starting from a similar initial composition and at constant conditions of 700 °C and 0.8 GPa for 10 Myr, the models show results with very different characteristics. The euhedral grain shows results similar to those predicted with a spherical assumption, largely preserving its original zoning. In contrast, the sub-euhedral grain shows significant re-equilibration, nearly erasing completely its initial zoning. This behaviour is caused by the high connectivity with the matrix. In addition to providing a robust solver for 3D diffusion modelling, these results demonstrate the role of grain geometry and matrix connectivity on intra-grain diffusion and highlight the power of 3D approaches to properly study the complexity of natural grains.

1. Introduction

Garnet is a common mineral in metamorphic rocks and often exhibits chemical zoning within individual grains (Atherton and Edmunds, 1966; Evans, 1965; Baxter et al., 2013; Rubatto et al., 2020). This zoning results primarily from variations in pressure (P) and temperature (T) conditions as well as the availability of elements during growth (Hollister, 1966; Spear et al., 1984; Tracy et al., 1976). Chemical zoning is often altered by syn- and post-growth intracrystalline diffusion when the temperature remains above a certain threshold for a sufficient duration, with the extent of modification depending on the cooling rate and the specific element of interest (Yardley, 1977; Woodsworth, 1977; Dempster, 1985; Li et al., 2018). Consequently, diffusion has been used to constrain the rate and duration of geological processes, leading to the development of diffusion chronometry, which has been applied extensively to garnet (Lasaga, 1983; Ganguly et al., 1996, 2000; Faryad and Chakraborty, 2005; Ague and Baxter, 2007; Devoir et al., 2021; Cheng et al., 2020; Spear, 2014). In these studies, numerical modelling has proven to be an efficient tool to retrieve geological constraints. In this particular case, an initial zoning pattern and (P–)T conditions are assumed, and time constraints are obtained by forward modelling under the assumption that the observed zoning pattern is dominantly controlled by post-growth diffusion. Numerous forward numerical models have also been successfully developed to account for both growth and syn- to post-diffusion of major elements in garnets (e.g. Caddick et al., 2010; Florence and Spear, 1991). In these models, garnet is often approximated as a growing sphere composed of concentric shells with different compositions, such as in the software Theria_G (Gaidies et al., 2008) and CZGM (Faryad and Ježek, 2019). The garnet composition in this case is obtained using phase equilibrium modelling. Diffusion between growth steps is then modelled using spherical coordinates along a fixed P–T path through time (t).

While spherical symmetry is a common and reasonable assumption, given that euhedral garnets typically form as regular dodecahedra, natural garnet grains often deviate from this ideal shape. This can be due to

---

* Corresponding author at: Institute of Geosciences, Johannes Gutenberg University, Mainz 55099, Germany.
E-mail address: hdomingu@uni-mainz.de (H. Dominguez).

https://doi.org/10.1016/j.cageo.2025.106023
Received 25 March 2025; Received in revised form 29 July 2025; Accepted 30 July 2025

many commonly occurring processes, such as syn- or post-deformation during growth, dissolution–precipitation, partial equilibrium, resorption or entrapment of inclusions (e.g. Ague and Carlson, 2013; Carlson, 2002; Storey and Prior, 2005; Baxter et al., 2017; Lanari et al., 2017; Konrad-Schmolke et al., 2007; Manzotti et al., 2024). To properly model these grains, it is necessary to develop numerical frameworks that do not use idealised shapes, but instead use realistic and complex geometries. Recent studies have modelled multicomponent diffusion in 3D in garnet using a dodecahedra shape (Gaidies et al., 2022) and linear trace element diffusion in garnet using complex geometries (Wu et al., 2025). These studies used finite element method (FEM) to explore the impact of assuming an ideal geometry on diffusion chronometry compared to more complex geometries. However, the impact of more complex boundary conditions on major element garnet composition involving both matrix and inclusions still need to be assessed for natural garnet geometries. This requires the ability to retrieve natural garnet geometries consistently. It also requires the development of new efficient numerical methods and tools to solve multicomponent diffusion in 3D Cartesian coordinates to be able to explore different geological scenarios with a reasonable total run time.

A popular approach to obtain 3D imaging of rock sample is micro-computed tomography (μCT). This approach allows individual minerals to be segmented from their surrounding matrix and inclusions based on density contrasts (Ketcham and Carlson, 2001). Micro-computed tomography imaging has been successfully applied to garnets in metamorphic rocks, allowing grain-size distribution analyses and providing insights into garnet growth and dissolution processes (e.g. Hartmeier et al., 2024; George and Gaidies, 2017; Li et al., 2024). This study focuses on developing a framework for modelling multicomponent major element post-growth diffusion in garnet using real grain geometries extracted from μCT. First, we present two natural garnet geometries segmented from μCT scans. Using a real chemical profile as a reference, we generate 3D chemical compositions to serve as initial conditions for diffusion modelling. We then present DiffusionGarnet.jl (Dominguez, 2023), a Julia package designed for 3D multicomponent diffusion simulation in garnet using finite differences. This package takes advantage of the Julia programming language and GPU acceleration to produce efficient simulations. Furthermore, we introduce the use of time-stepping algorithms called stabilised explicit Runge–Kutta methods and demonstrate the efficiency of stabilised explicit methods for this type of problem. The simulations also highlight the potential role of matrix connectivity in modifying garnet composition during diffusion. This paves the way for a better understanding of garnet-matrix interactions in the case of complex scenarios and different garnet geometries.

2. Governing equations

The theoretical framework for multicomponent diffusion used in this study is an extension of Fick's Second law (Onsager, 1945; Fick, 1855), incorporating the reciprocal relationships of non-equilibrium thermodynamics (Onsager, 1931a,b) and assuming spatially uniform temperature and pressure conditions (Lasaga, 1979). For garnet, four different components are considered here, corresponding to the primary endmembers of the garnet solid solution: Mg, Fe, Mn, and Ca. Using the electroneutrality condition, the system of equations can be formulated as a set of $p-1$ coupled non-linear parabolic partial differential equations (PDEs), where p is the number of components, here equal to four (Lasaga, 1979). This can be written, for one component i, in Cartesian coordinates, as:

$$\frac{\partial C_i}{\partial t} = \vec{\nabla} \cdot \sum_{j=1}^{p-1} D_{ij} \vec{\nabla} C_j, \tag{1}$$

where C_i is the molar fraction of the ith component in the compositional vector $\vec{C}$ and D_{ij} is a component of the $(p-1)\times(p-1)$ interdiffusion coefficient matrix $\mathbf{D}$ ($\mathrm{m^2\ s^{-1}}$), t is the time (s) and $\vec{\nabla}$ is the differential operator ($\mathrm{m^{-1}}$). The fixed component is defined here as Ca. Note that the use of molar fraction supposes a constant molar volume in garnet (e.g. Lasaga, 1983).

The components of $\mathbf{D}$ can be approximated, under the assumption of ideal behaviour for equally charged cation diffusion in a silicate framework, as:

$$D_{ij} = D_i^* \delta_{ij} - \frac{C_i D_i^*}{\sum_{k=1}^{p} C_k D_k^*}\left(D_j^* - D_n^*\right), \tag{2}$$

with D_i^* the tracer diffusion coefficient ($\mathrm{m^2\ s^{-1}}$) of the ith component, δ_{ij} the Kronecker delta, and D_p^* the tracer diffusion coefficient of the dependent component (here Ca) (Lasaga, 1979).

To obtain a closed system, an expression for D_i^* is needed and can be obtained experimentally, assuming an Arrhenius relationship with a temperature and pressure dependency:

$$D_i^* = D_{0,i} \exp\left(-\frac{Ea_i - (P - P_0)\Delta V_i^+}{RT}\right), \tag{3}$$

with $D_{0,i}$ the pre-exponential constant ($\mathrm{m^2\ s^{-1}}$), Ea_i the activation energy of diffusion ($\mathrm{J\ mol^{-1}}$), ΔV_i^+ the activation volume of diffusion ($\mathrm{m^3\ mol^{-1}}$) for the i component and P_0 the pressure of calibration (Pa), R the universal gas constant ($\mathrm{kg\ m^2\ s^{-2}\ K^{-1}\ mol^{-1}}$), T the temperature (K) and P the pressure (Pa) of interest.

Eq. (1) can be solved numerically with Eqs. (2) and (3), if appropriate boundary and initial conditions are defined. The ones used in this study in the case of the 3D models are described in the following section.

3. Methods

3.1. Analytical methods and post-processing

In order to use realistic garnet morphologies for the 3D numerical models, two natural garnet porphyroblasts of similar size were selected to be used as starting geometry. These two grains are amphibolite facies garnets from the same metapelitic rock sample from the Val Piora locality, Central Alps, Switzerland. The two garnets were hand-picked in the field and selected to have two different end-members: a well-shaped, euhedral garnet grain, hereafter referred as the euhedral garnet, and a deformed sub-euhedral poikiloblastic garnet grain, hereafter referred as the sub-euhedral garnet. Each individual grain was then imaged in 3D at high resolution (∼5 μm voxel size) using μCT with a BRUKER SkyScan 1273 3D X-ray microscope at the Institute of Geological Sciences, University of Bern. A micro-focus X-ray tube with an acceleration voltage of 100 kV and a beam current of 80 μA was used as the source. The X-ray beam was filtered using a 2.0 mm Cu plate. The exposure time of the CCD detector was set to 271 ms, and averaging of 10 frames was used for noise reduction. The sample was rotated stepwise by 0.15° in the beam cone. The resulting tomography data were reconstructed using the NRecon software with corrections for beam hardening and misalignment artifacts. Finally, the data was imported into the Dragonfly software (Gendron et al., 2021) to segment the garnet grains from their inclusions and the matrix. The data was segmented using intensity thresholds and a region of interest (ROI) was created for the largest 6-connected garnet domain for each grain. This ROI was then downsampled in Dragonfly to resolutions of 768^3, 564^3 and 256^3 to be used in the 3D numerical models. Since the initial domains of the two scans are not cubic but slightly shorter in the z-direction, this resulted in a regular grid with cuboids shorter in the z-axis rather than voxels. These ROIs were then exported as 3D binary matrices.

3.2. Initial and boundary conditions

To define the initial and boundary conditions to solve for Eq. (1), additional steps are required: assigning a composition to each cuboid in

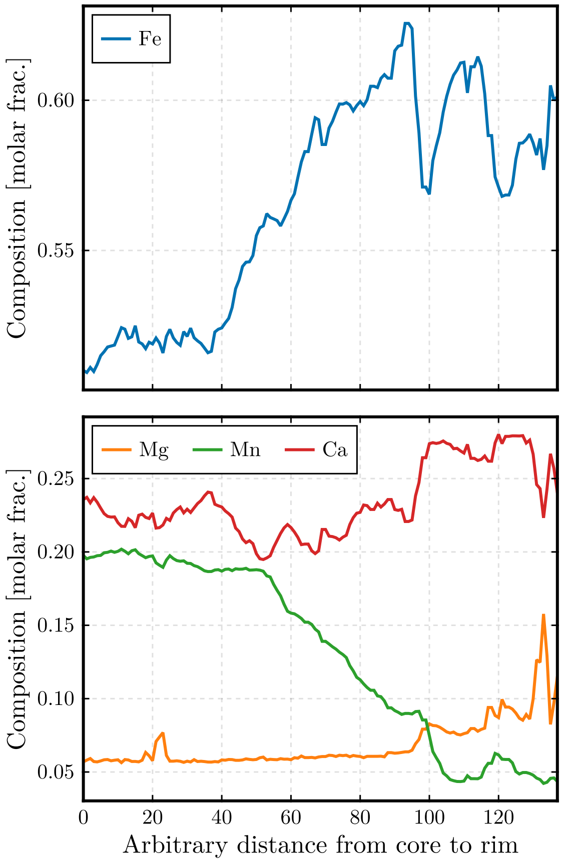

Fig. 1. Initial composition of the garnet composition used for interpolation in 3D. This is a core to rim profile obtained from compositional maps using XMapTools (see text). The composition at the rim is assumed to represent the equilibrium garnet composition at peak conditions and was applied as the boundary condition in contact with the matrix.

the garnet domain (Ω_{Grt}), locating the boundaries of Ω_{Grt}, and setting the boundary conditions. These steps were performed using the Julia programming language (Bezanson et al., 2017) and are described in the following.

The conversion of garnet density from µCT data directly to composition was not possible due to the small density variations and the lack of a suitable density calibration. Furthermore, since the goal of this study was to investigate the effects of chemical diffusion in the context of 3D geometries, it was important to have similar initial chemical conditions for both grains. To achieve this, a 3D composition was numerically generated from natural data and mapped onto the 3D garnet grain geometries. To do so, a high resolution chemical profile was obtained from quantitative compositional maps using the strip tool implemented in XMapTools (Lanari et al., 2019, 2014; Lanari and Tedeschi, 2025), and interpolated in 3D over the grains assuming an ellipsoid shape. The initial chemical profile used is shown in Fig. 1 and is from an almandine rich blueschist facies garnet from a mafic sample of Cazadero, Franciscan Complex, USA (Sample AUS in Cesare et al., 2019). This profile was chosen because it is showing prominent and sharp zoning, with a composition typical of a low-T garnet (see Supplementary Material S1 for the chemical zoning on the original garnet). The ellipsoid shape is a reasonable assumption, as euhedral garnets are often approximated as spheres (e.g. Gaidies et al., 2008; Faryad and Ježek, 2019), and a deformed sphere can be described as an ellipsoid in the case of pure and simple shear deformation.

To define the best fitting ellipsoid for each garnet grain, three parameters were required: the principal axes' directions and magnitudes, as well as the ellipsoid centre. The centre of each ellipsoid was assumed to be the centre of mass of Ω_{Grt} and the inclusion domain (Ω_{I}, defined later in this section), and the main axes of the inertia tensor ($\mathbf{I}$) were used as principal directions for the ellipsoid axes. The centre of mass was calculated in the discrete space, assuming a constant density for Ω_{Grt}, according to the equation:

$$\overrightarrow{cm} = \frac{1}{G} \cdot \sum_{k=1}^{G} \overrightarrow{v_k}, \tag{4}$$

where $\overrightarrow{cm}$ is the centre of mass, G is the total number of garnet grid point, and $\overrightarrow{v_l}$ is the position vector of each k garnet grid point. The expression is valid for grid point of constant size. Using $\overrightarrow{cm}$ as the origin of a new coordinate system, $\mathbf{I}$ can be calculated (e.g. Hand and Finch, 1998, p. 286):

$$\mathbf{I} = m \cdot \begin{bmatrix} \sum_{l=1}^{N}(y_l'^2 + z_l'^2) & -\sum_{l=1}^{N} x_l' y_l' & -\sum_{l=1}^{N} x_l' z_l' \\ -\sum_{l=1}^{N} x_l' y_l' & \sum_{l=1}^{N}(x_l'^2 + z_l'^2) & -\sum_{l=1}^{N} y_l' z_l' \\ -\sum_{l=1}^{N} x_l' z_l' & -\sum_{l=1}^{N} y_l' z_l' & \sum_{l=1}^{N}(x_l'^2 + y_l'^2) \end{bmatrix}, \tag{5}$$

where x', y' and z' are the 3D Cartesian coordinates in a reference frame with $\overrightarrow{cm}$ as the origin and m is the mass of the object, here set to 1. The directions of the eigenvectors of $\mathbf{I}$ correspond to the principal axes of inertia, and are used to define the direction of the major axes of the ellipsoid for each garnet domain. To obtain the magnitude of each axis that would best fit the ellipsoid to the garnet domain shape, an iterative approach was used. An initial ellipsoid was defined with axis magnitudes deliberately smaller than those of the garnet domain of interest. For each garnet grid point located outside of this ellipsoid, the major axis closest in angle to the garnet grid point was increased by 1% until all garnet grid points were located inside the ellipsoid. From this ellipsoid, the original chemical profile was then scaled to the ellipsoid shape, and the composition for each garnet grid point was determined by linear interpolation from it. The initial compositions for the euhedral and sub-euhedral grains are shown in Figs. 2 and 3, respectively.

Concerning the boundary conditions of Ω_{Grt}, two different types were defined for both garnet grain geometries:

- Matrix boundary ($\partial\Omega_{\text{Grt}}^{M}$), the interface where Ω_{Grt} is in contact with the surrounding matrix domain (Ω_M), which is an open domain encompassing Ω_{Grt}
- Inclusion boundary ($\partial\Omega_{\text{Grt}}^{I}$), the interface where the garnet is in contact with inclusions (Ω_I), representing closed sub-domains within Ω_{Grt}

Additionally, from the sub-euhedral grain geometry, a second model referred as the isolated matrix model was defined, with an additional boundary associated with a third domain:

- Internal matrix boundary ($\partial\Omega_{\text{Grt}}^{M\Subset\text{Grt}}$): the boundary between the garnet grain and a connected matrix domain contained inside the sub-euhedral garnet grain ($\Omega_{M\Subset\text{Grt}}$)

To properly locate $\partial\Omega_{\text{Grt}}^{M}$, $\partial\Omega_{\text{Grt}}^{I}$ and $\partial\Omega_{\text{Grt}}^{M\Subset\text{Grt}}$, it was first required to define Ω_I, Ω_M and $\Omega_{M\Subset\text{Grt}}$ from the ROIs, as only Ω_{Grt} is represented in the original binary 3D matrix data. A flood fill algorithm was implemented in 3D and used to define Ω_M (e.g. Newman and Sproull, 1979, p. 253). The inclusion domain was then defined from the remaining, unclassified regions. For $\Omega_{M\Subset\text{Grt}}$ in the isolated matrix model, the same ellipsoid used for defining the initial conditions was used to replace Ω_M contained inside the ellipsoid by $\Omega_{M\Subset\text{Grt}}$. This new domain was then eroded in contact to Ω_M until it was visually contained inside Ω_{Grt}. This step was normalised by the number of pixels so that similar results could be obtained at different resolutions. This approach allowed $\Omega_{M\Subset\text{Grt}}$ to have a similar shape relative to the sub-

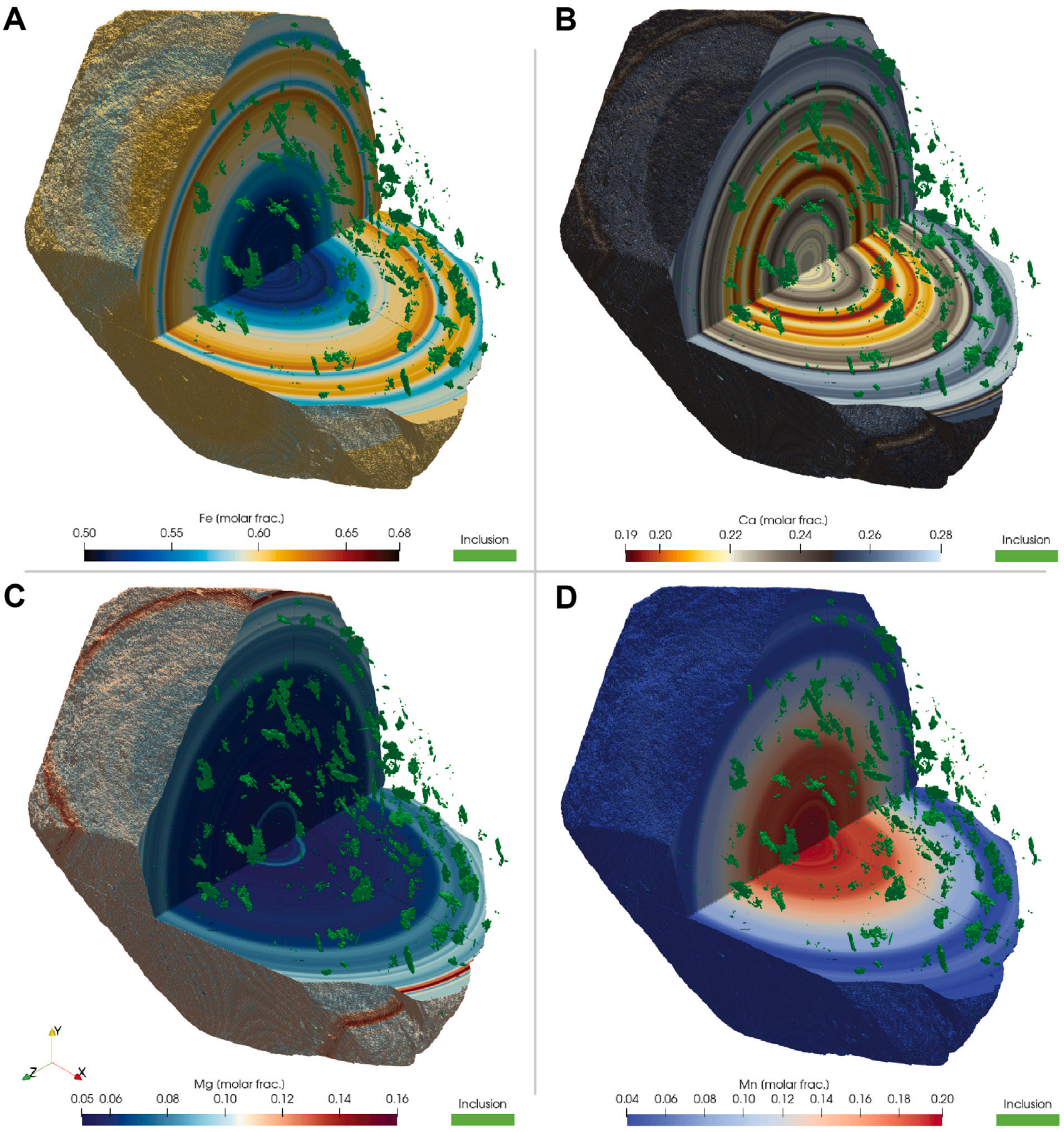

Fig. 2. Initial conditions for the 3D euhedral garnet geometry, with the inclusion domain shown in green. The resolution shown is 768^3. The size of the domain is $10.4 \times 10.4 \times 7.8$ mm. A quarter of the grain is removed for visualisation. (A) Fe composition. (B) Ca composition. (C) Mg composition. (D) Mn composition. All compositions are obtained from interpolating a measured profile (see Fig. 1) onto a fitted ellipsoid.

euhedral grain geometry. The different domains for the three model setups are shown in Fig. 4.

The boundaries $\partial\Omega^{M}_{\mathrm{Grt}}$, $\partial\Omega^{I}_{\mathrm{Grt}}$ and $\partial\Omega^{M \Subset \mathrm{Grt}}_{\mathrm{Grt}}$ were finally obtained by finding and mapping the intersections between Ω_{Grt} and Ω_M, Ω_{Grt} and Ω_I and Ω_{Grt} and $\Omega_{M \Subset \mathrm{Grt}}$, respectively. Two different boundary conditions were defined. For $\partial\Omega^{M}_{\mathrm{Grt}}$, a Dirichlet boundary condition was enforced, with the composition fixed to $\overrightarrow{C^{\mathrm{eq}}}$, the composition vector of the garnet composition in equilibrium with the matrix. For $\partial\Omega^{I}_{\mathrm{Grt}}$, a homogeneous Neumann boundary condition was applied, implying no chemical exchange between the inclusions and the garnet. For $\partial\Omega^{M \Subset \mathrm{Grt}}_{\mathrm{Grt}}$ in the second model of the sub-euhedral grain, a homogeneous Neumann boundary condition was similarly applied.

This can be formulated in 3D in mathematical notation as:

$$
\begin{aligned}
\frac{\partial \vec{C}}{\partial x}\bigg|_{\vec{X} \in \partial\Omega^{I}_{\mathrm{Grt}}} &= \frac{\partial \vec{C}}{\partial x}\bigg|_{\vec{X} \in \partial\Omega^{M \Subset \mathrm{Grt}}_{\mathrm{Grt}}} = 0, && \text{for } \vec{X} \pm \vec{e}_1 \in \Omega_I, \text{or} \\
& && \quad \vec{X} \pm \vec{e}_1 \in \Omega_{M \Subset \mathrm{Grt}}, \\
\frac{\partial \vec{C}}{\partial y}\bigg|_{\vec{X} \in \partial\Omega^{I}_{\mathrm{Grt}}} &= \frac{\partial \vec{C}}{\partial y}\bigg|_{\vec{X} \in \partial\Omega^{M \Subset \mathrm{Grt}}_{\mathrm{Grt}}} = 0, && \text{for } \vec{X} \pm \vec{e}_2 \in \Omega_I, \text{or} \\
& && \quad \vec{X} \pm \vec{e}_2 \in \Omega_{M \Subset \mathrm{Grt}}, \\
\frac{\partial \vec{C}}{\partial z}\bigg|_{\vec{X} \in \partial\Omega^{I}_{\mathrm{Grt}}} &= \frac{\partial \vec{C}}{\partial z}\bigg|_{\vec{X} \in \partial\Omega^{M \Subset \mathrm{Grt}}_{G}} = 0, && \text{for } \vec{X} \pm \vec{e}_3 \in \Omega_I, \text{or} \\
& && \quad \vec{X} \pm \vec{e}_3 \in \Omega_{M \Subset \mathrm{Grt}}, \\
\vec{C}\bigg|_{\vec{X} \in \partial\Omega^{M}_{\mathrm{Grt}}} &= \overrightarrow{C^{\mathrm{eq}}}, && \text{for } \vec{X} \pm \vec{e}_m \in \Omega_M, \quad m \in \{1, 2, 3\},
\end{aligned}
\tag{6}
$$

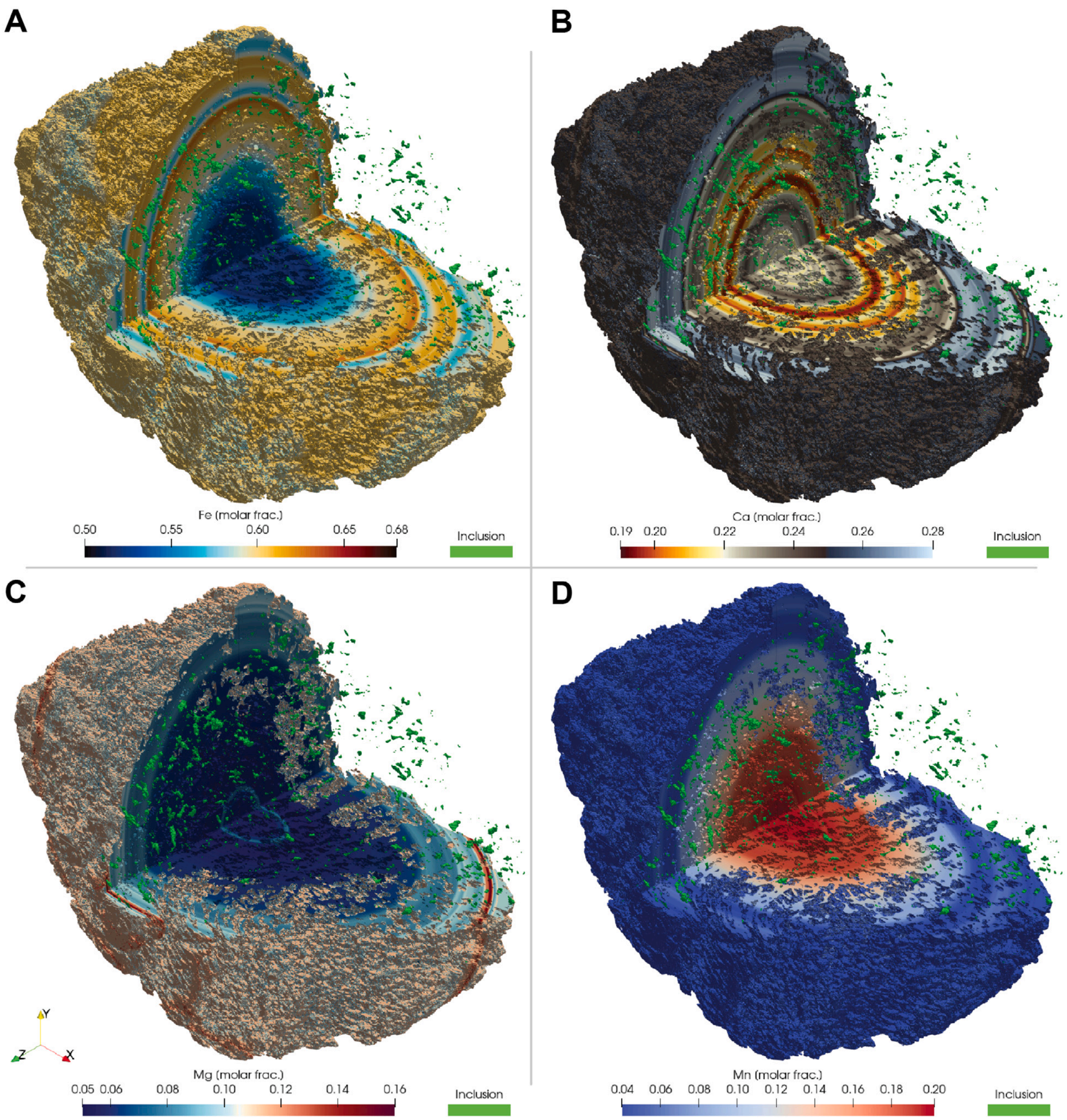

Fig. 3. Initial conditions for the 3D sub-euhedral garnet geometry, with the inclusion domain shown in green. The resolution shown is 768^3. The size of the domain is $11.4 \times 11.4 \times 7.6$ mm. A quarter of the grain is removed for visualisation. (A) Fe composition. (B) Ca composition. (C) Mg composition. (D) Mn composition. All compositions are obtained from interpolating a measured profile (see Fig. 1) onto a fitted ellipsoid.

where x, y, z are the Cartesian coordinates, $\overrightarrow{X}$ is the position vector of grid points in the computational domain and $\vec{e}_m$ are the Cartesian unit basis vectors in the mth direction.

The petrological rationale for defining $\overrightarrow{C}$ at Ω^{M}_{Grt} is that the matrix and garnet boundaries remain in local equilibrium over diffusion timescales. For $\overrightarrow{C}$ at Ω^{I}_{Grt}, this implies that the inclusion phases either (i) do not contain Mg, Fe, Mn, or Ca, such as quartz, or (ii) have significantly lower diffusion rates for these elements compared to garnet, preventing any exchange between Ω_{Grt} and Ω_I within the timescales of interest. This is a similar reasoning concerning $\overrightarrow{C}$ at $\partial\Omega_G^{M\Subset\text{Grt}}$, where $\Omega_{M\Subset\text{Grt}}$ is considered to have a low connectivity, preventing good exchange and local equilibrium with the outside matrix.

3.3. Non-dimensionalisation and numerical approach

Using Eqs. (1), (2), (3), (6) and the initial conditions, the system of PDEs can be numerically solved. To mitigate numerical errors and insuring better convergence, the system was first non-dimensionalised. As the compositions are already dimensionless, only time and space need special treatment. Taking the characteristic length ($\tilde{L}$) as the

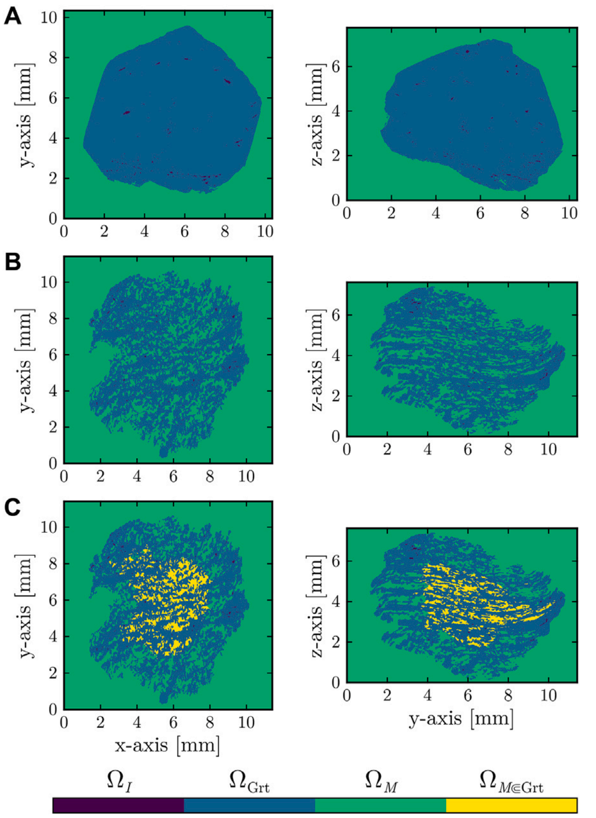

Fig. 4. Central sections of the garnet grains showing the domains distribution for the three model setups. The resolution shown is 768^3. (A) Euhedral garnet model (EGM). (B) Open garnet model (OGM). (C) Isolated Matrix Model (IMM), derived from the same geometry as OGM. The left panels show sections normal to the z-axis, while the right panels show sections normal to the x-axis. The notations Ω_I, Ω_{Grt}, Ω_M and $\Omega_{M\in\mathrm{Grt}}$ refer to the inclusion domain, the garnet domain, the matrix domain, and the isolated matrix domain, respectively.

length of the domain in the x-axis (L_x), and the characteristic diffusion $\tilde{D}$ as the mean of the initial tracer diffusion coefficients, the characteristic variables can be defined as:

$$
\begin{aligned}
\tilde{L} &= L_x,\\
\tilde{D} &= \frac{D^*_{\mathrm{Mg}} + D^*_{\mathrm{Fe}} + D^*_{\mathrm{Mn}} + D^*_{\mathrm{Ca}}}{4},\\
\tilde{\mathbf{D}} &= \frac{\mathbf{D}}{\tilde{D}},\\
\tilde{t} &= \frac{\tilde{L}^2}{\tilde{D}},
\end{aligned}
\tag{7}
$$

where $\tilde{\mathbf{D}}$ is the dimensionless interdiffusion coefficient matrix and $\tilde{t}$ is the characteristic time (s). Using Eq. (1) and the scaling variables for all $p-1$ components, we obtain:

$$
\begin{aligned}
\frac{\partial C_{\mathrm{Mg}}}{\partial \tilde{t}} &= \tilde{\nabla} \cdot \tilde{D}_{\mathrm{MgMg}} \tilde{\nabla} C_{\mathrm{Mg}} + \tilde{\nabla} \cdot \tilde{D}_{\mathrm{MgFe}} \tilde{\nabla} C_{\mathrm{Fe}} + \tilde{\nabla} \cdot \tilde{D}_{\mathrm{MgMn}} \tilde{\nabla} C_{\mathrm{Mn}},\\
\frac{\partial C_{\mathrm{Fe}}}{\partial \tilde{t}} &= \tilde{\nabla} \cdot \tilde{D}_{\mathrm{FeMg}} \tilde{\nabla} C_{\mathrm{Mg}} + \tilde{\nabla} \cdot \tilde{D}_{\mathrm{FeFe}} \tilde{\nabla} C_{\mathrm{Fe}} + \tilde{\nabla} \cdot \tilde{D}_{\mathrm{FeMn}} \tilde{\nabla} C_{\mathrm{Mn}},\\
\frac{\partial C_{\mathrm{Mn}}}{\partial \tilde{t}} &= \tilde{\nabla} \cdot \tilde{D}_{\mathrm{MnMg}} \tilde{\nabla} C_{\mathrm{Mg}} + \tilde{\nabla} \cdot \tilde{D}_{\mathrm{MnFe}} \tilde{\nabla} C_{\mathrm{Fe}} + \tilde{\nabla} \cdot \tilde{D}_{\mathrm{MnMn}} \tilde{\nabla} C_{\mathrm{Mn}},
\end{aligned}
\tag{8}
$$

with $\tilde{\nabla} = \frac{1}{\tilde{L}}\nabla$.

As this system is composed of stiff non-linear coupled PDEs, it is not trivial to solve numerically at high resolution in 3D efficiently. For that reason, a Julia package, DiffusionGarnet.jl (Dominguez, 2023), was developed. Designed for high performance, it leverages Julia's package ecosystem and supports parallel computing on both CPUs and GPUs. The package also allows performing multicomponent major element diffusion in garnet in spherical, 1D and 2D Cartesian coordinates.

The numerical approach used in DiffusionGarnet.jl to solve Eq. (8) is based on the method of lines (e.g. Schiesser, 2012). In this approach, the system of PDEs is first discretised in space to form a semi-discretised form composed of ordinary differential equations (ODEs). This form is then solved over time using standard, well-established ODE solvers. In DiffusionGarnet.jl, spatial discretisation is performed using conservative finite differences.

While FEM offers advantages in handling complex geometries (e.g. Wu et al., 2025), the use of finite differences in this study is motivated by two main considerations. Firstly, one of the primary goal is to achieve high performance in 3D simulations using GPU acceleration. The finite element method typically involves mesh assembly and more complex data structures, which hinder efficient GPU implementation due to non-local memory access and communication overheads between the CPU and GPU. In contrast, finite differences map naturally onto regular grids, enabling efficient memory access patterns and parallelism on modern GPU architectures. Secondly, the garnet geometries used in this study are derived from µCT scans and are therefore voxel-based by nature. These voxel models can be used directly on a regular grid, eliminating the need for remeshing, a computationally expensive step in 3D that introduces additional complexity. Given these factors, finite differences provide a practical and efficient solution in this context.

Since the system consists of three parabolic PDEs, the spatial discretisation process leads to a system of $3 \times N$ ODEs, where N is the number of grid points. Temporal discretisation is then handled using a stabilised explicit Runge–Kutta method. This family of time-stepping algorithms was specifically developed for solving large systems of mildly stiff parabolic PDEs (Sommeijer et al., 1998; Van Der Houwen and Sommeijer, 1980). These solvers extend the stability domain of standard explicit methods, which is bounded by the classical Courant–Friedrich–Lewy (CFL) condition (Courant et al., 1928). As a result, timestep (Δt) can approach those of implicit methods without the computational cost of constructing and solving a linear (and possibly non-linear) system at each Δt. Furthermore, because these are explicit methods, they are inherently well-suited for parallelisation, as they involve matrix-free operations. Finally, stabilised explicit solvers have a workload that scales theoretically linearly with numerical resolution Δx (i.e. $\mathcal{O}(n)$ in big O notation) (e.g. Abdulle et al., 2022). This contrasts with standard explicit methods, where the number of timesteps scales almost quadratically due to the CFL condition ($\mathcal{O}(n^{1+2/d})$, with d the number of dimensions, in this case 3). This makes them particularly effective for high-resolution, large-scale models (e.g. Dumont et al., 2013). A common step of stabilised explicit methods is the use of internal stages using shifted Chebyshev polynomials to extend the domain of stability of the numerical solution in the negative real axis (Hairer and Wanner, 1996, pp. 31–36). The interested reader can refer to Abdulle (2015) for a comprehensive introduction on stabilised explicit methods. Different solvers have been proposed and differ in the way the polynomials or the Runge–Kutta steps are constructed. To evaluate the performance of some of them for multicomponent diffusion, five different stabilised explicit methods were tested at varying resolutions: RKC, SERK2v2, ROCK2, ROCK4 and ESERK5 (Sommeijer et al., 1998; Kleefeld and Martín-Vaquero, 2013; Abdulle and Medovikov, 2001; Abdulle, 2002; Martín-Vaquero and Kleefeld, 2019). The solvers RKC, SERK2v2, and ROCK2 are second order methods, whereas ROCK4 and ESERK5 are fourth and fifth order methods, respectively. In addition, to better estimate their performance against more conventional time-stepping methods, an explicit second order Runge–Kutta (RK2) method using an embedded Euler method for adaptive time stepping was also used (e.g. Hairer et al., 1993, pp. 132–133). The specificity and details of the implementation of each method is beyond the scope of this study, but the interested reader can refer to the

Table 1
Summary of the parameters used in the numerical models: Euhedral Garnet Model (EGM), Open Garnet Model (OGM), and Isolated Matrix Model (IMM). Both OGM and IMM have the same grain geometry.

Parameter	Symbol	EGM	OGM	IMM
Pressure condition	P	0.7 GPa	0.7 GPa	0.7 GPa
Temperature condition	T	700 °C	700 °C	700 °C
Total time	t	10 Myr	10 Myr	10 Myr
Total length in x and y	L_x	10.4 mm	11.4 mm	11.4 mm
Total length in z	L_z	7.8 mm	7.6 mm	7.6 mm
Internal matrix domain	$\Omega_{M \Subset \mathrm{Grt}}$	No	No	Yes

original works for more details. These solvers are implemented in the DifferentialEquations.jl package (Rackauckas and Nie, 2017), an ODE solver ecosystem. This provides a way to compare ODE solvers with consistent implementations between the different algorithms.

Additionally, spatial discretisation is handled with ParallelStencil.jl (Omlin and Räss, 2022), which allows to write architecture-agnostic code compatible for efficient parallelisation on both CPUs and GPUs. As such, models in DiffusionGarnet.jl can be performed on CPUs or GPUs with minimal modification of the code. Finally, Unitful.jl (Keller and Contributors, 2025) is used for units handling and GeoParams.jl (Kaus et al., 2025) for calculating the tracer diffusion coefficients.

All models were performed on an NVIDIA GH200 Grace Hopper Superchip at the Johannes Gutenberg University, Mainz, using single-precision floating-point arithmetic (float32). This superchip contains 96 GB of GPU memory (GRAM) along with 480 GB of RAM. It was also used to compare models at different resolutions running only on CPU or with GPU acceleration. Concerning the simulations involving GPU acceleration, all relevant data structures, such as initial conditions, diffusion coefficients, and caches from the numerical solvers were directly allocated at the beginning of the simulation in GPU memory using Compute Unified Device Architecture (CUDA) arrays (Besard et al., 2018). The numerical operations, including spatial discretisation and time stepping stages, were then performed on the GPU, using GPU kernels. This ensured that both data storage and computations remained on the GPU, minimising memory transfer overhead between the CPU and GPU.

The visualisations were generated using the Julia package Makie.jl (Danisch and Krumbiegel, 2021) for 1D and 2D views, while ParaView (Ahrens et al., 2005) was used for 3D representations.

4. Results and discussion

Three different model configurations were defined and used: the euhedral garnet model (EGM), the open garnet model (OGM), and the isolated matrix model (IMM). Both OGM and IMM share the same garnet geometry, corresponding to the sub-euhedral garnet grain. However, IMM includes $\Omega_{M \Subset \mathrm{Grt}}$ as a domain. The chosen P–T–t conditions for all models are 700 °C and 0.8 GPa, held constant over 10 Myr, which correspond to upper amphibolite conditions during Barrovian-like regional metamorphism. The D_i^* values used for Mg, Fe and Mn are from Chakraborty and Ganguly (1992), and the tracer diffusion coefficient of Ca is fixed to $0.5 \times D_{\mathrm{Fe}}^*$, following the approach of Loomis et al. (1985). The principal parameters and characteristics of the models are summarised in Table 1.

4.1. *Performance of the numerical models and evaluation of the stabilised explicit methods*

Efficient performance in 3D numerical models is essential for exploring multiple geological scenarios, systematics, and performing inverse modelling tasks such as diffusion chronometry. These applications often require running large numbers of forward models to explore the parameter space or quantify uncertainty (e.g. Mutch et al., 2021; Shea et al., 2015). Consequently, the development and implementation of computationally efficient numerical methods is needed.

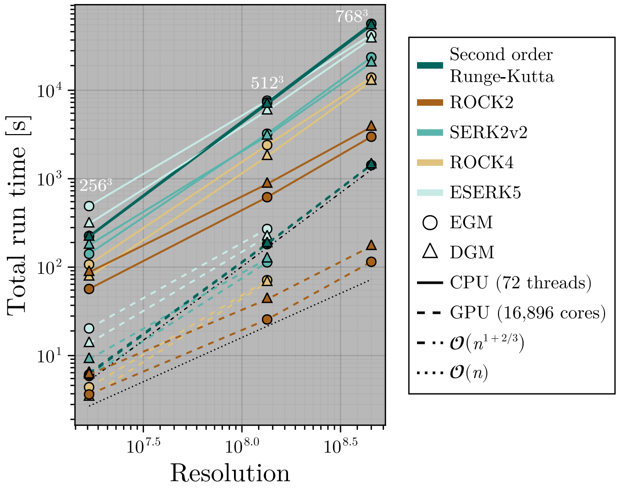

Fig. 5. Total run time of the euhedral garnet model (EGM) and the open garnet model (OGM) at three different resolutions in 3D: 256^3, 512^3 and 768^3. Each colour corresponds to a different explicit solver used for the simulation. The solvers ROCK2, SERK2v2, ROCK4 and ESERK5 (Abdulle and Medovikov, 2001; Kleefeld and Martín-Vaquero, 2013; Abdulle, 2002; Martín-Vaquero and Kleefeld, 2019) are all stabilised explicit methods whereas the standard explicit second order Runge–Kutta method (RK2) is used as a reference model. Each simulation was performed both with and without GPU acceleration and utilising 72 CPU threads. At the resolution of 768^3, only ROCK2 and RK2 methods were able to fit the GRAM of the GPU. For total run-time below 10 min, the models were run twice for each run, to exclude the precompilation time. Above this threshold, the precompilation time was considered negligible with respect to the total run-time. The dark dotted lines represent the theoretical algorithmic scalings of explicit and stabilised explicit methods for parabolic equations in 3D. All models were performed on an NVIDIA GH200 Grace Hopper Superchip using single-precision floating-point arithmetic (float32), OrdinaryDiffEqStabilizedRK 1.1.0, and Julia version 1.11.2.

As such, it is relevant to evaluate the performance of the five different stabilised explicit methods (RKC, SERK2v2, ROCK2, ROCK4 and ESERK5) compared to more conventional time-stepping algorithms, such as RK2. To do so, EGM and OGM were performed at three different resolutions: 768^3, 564^3 and 256^3 for each method. Each simulation was performed both with and without GPU acceleration and utilising 72 CPU threads. This was done to assess how garnet geometry influences computational performance. Due to GRAM limitations, only the 564^3 and 256^3 resolutions were tested across all methods on GPU. At 768^3, only RK2, ROCK2 and RKC could fit in memory. Furthermore, the RKC method did not converge above the resolution of 256^3 and was therefore discarded. As a consequence, its results are not reported in the following. The performance results are presented in Fig. 5. The results indicate that GPU acceleration consistently enhances computational speed, achieving a 20- to 30-fold speedup across all algorithms compared to the CPU-only approach. Among the tested methods, ROCK2 demonstrated the best overall performance for both models, highlighting its robustness. Compared to the standard explicit method RK2, all algorithms perform better at the highest resolution in the CPU-only approach and show a better algorithmic scaling. However, the ROCK2 algorithm is the only one to show a scaling close to $\mathcal{O}(n)$. Notably, with GPU acceleration at a resolution of 768^3, ROCK2 also achieved remarkable short total runtimes of just 115 s for EGM and 172 s for OGM, which is about an order of magnitude faster than with RK2. Furthermore, ROCK2 has lower memory requirements than SERK2v2, ROCK4 and ESERK5, making it an even more suitable choice in memory-constrained scenarios.

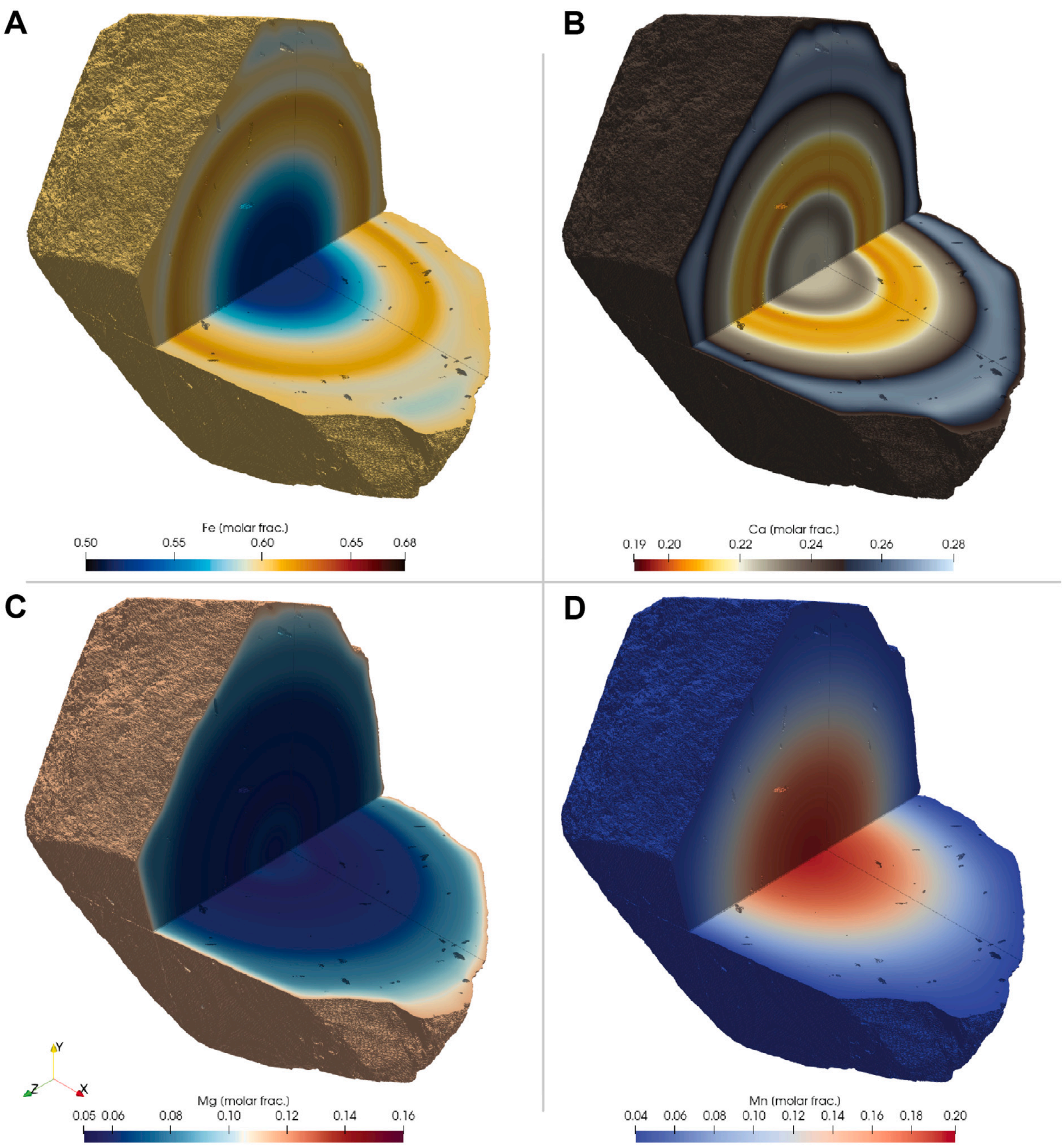

Fig. 6. Final timestep after 10 Myr of the euhedral garnet geometry model (EGM). A quarter of the grain is removed for visualisation. Temperature and pressure remain constant at 700 °C and 0.8 GPa. (A) Fe composition (B) Ca composition (C) Mg composition (D) Mn composition. The resolution is 768^3.

4.2. Comparison of the numerical models

Concerning the evolution of the garnet compositions for EGM, OGM, and IMM, the final state in 3D of each model for each element is shown in Fig. 6 (EGM), and Figs. 7 and 8 (OGM and IMM). To analyse composition evolution over time, central sections normal to the *z*-axis of all models for all elements are shown in Figs. 9 (Fe), 10 (Ca), 11 (Mg) and 12 (Mn). Finally, a 1D core-rim profile along the *x*-axis is shown for each model in Fig. 13. Additionally, time-lapse 3D videos for each model are available in the supplementary material of this article (Supplementary Material S2, S3, S4, S5, S6, S7, S8, S9, S10, S11).

Comparing the results of the three models highlights some important differences that reflect the variation in geometries and boundary conditions. After 10 Myr, EGM retains lots of the features from its original zoning (for instance with Ca and Fe in Figs. 6, 10A, 9A and 13A). This preservation is due to the absence of pathways connecting the matrix to the interior of the garnet, as the grain lacks fracturing or large inclusions in contact with the matrix. Consequently, strong gradients are only present from the original garnet composition rather than being induced by boundary conditions in the core and mantle of the grain, significantly limiting diffusion. In contrast, OGM shows

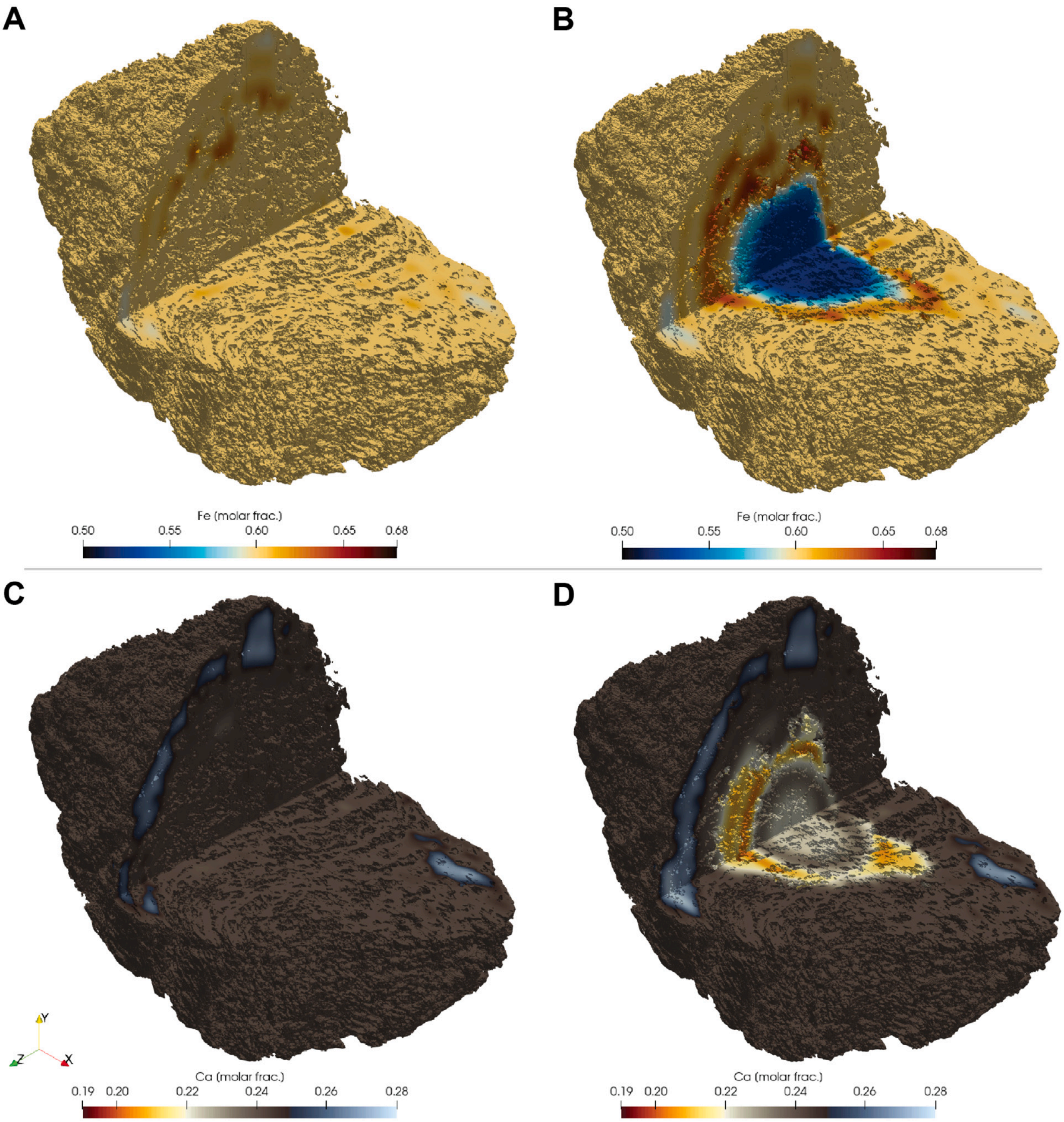

Fig. 7. Final timestep after 10 Myr for Fe (top) in (A) the open garnet model (OGM) and (B) the isolated matrix model (IMM), and for Ca (bottom) in (C) OGM and (D) IMM. A quarter of the grain is removed for visualisation. Temperature and pressure remain constant at 700 °C and 0.8 GPa. The initial setups from the two models differ only by their boundary conditions: the composition in the garnet is fixed to $\overline{C^{eq}}$ in contact with all the matrix ($\partial\Omega^{M}_{\mathrm{Grt}}$) in DMG. In contrast, in IMM, the garnet does not exchange chemically with the matrix near the core. The resolution is 768^3 for both models.

strong connectivity between the inside of the garnet and the surrounding matrix (Fig. 4B). As a result, equilibration occurs rapidly, erasing most of the original compositional features within just 1 Myr (see for instance Fe and Mg content in Figs. 9B, 11B and 13B). Patchy zoning persists only in areas where the matrix has limited contact with the garnet, as seen for Ca and Mg in the outer rim of the grain (Figs. 7C and 8A). For Mn, the fastest diffusing element, the zoning is completely erased (Figs. 12B and 8C). Concerning IMM, it shows an intermediate result between EGM and OGM, with slow diffusion in the core, and fast diffusion in the mantle and in the rim of the grain (Fig. 13C). Moreover, remnants of the original zoning are preserved only in the region in contact with $\Omega^{M\in\mathrm{Grt}}_{\mathrm{Grt}}$ (Figs. 4C), resulting in patchy zoning patterns that deviate from the original concentric structure of the compositions, as seen for Fe and Ca (Figs. 7B, 9C, 7D and 10C). The Mn core is also preserved, contrary to OGM (Figs. 8C and D, and 12B and C).

4.3. *Uphill diffusion*

Another remarkable feature of the models is the occurrence of prominent uphill diffusion, in particular for Fe in OGM (Figs. 9B at 0.1 and 1.0 Myr and 13B in the whole profile) and IMM (Figs. 9B at 0.1 and 1.0 Myr and 13C, especially at the distances from the core

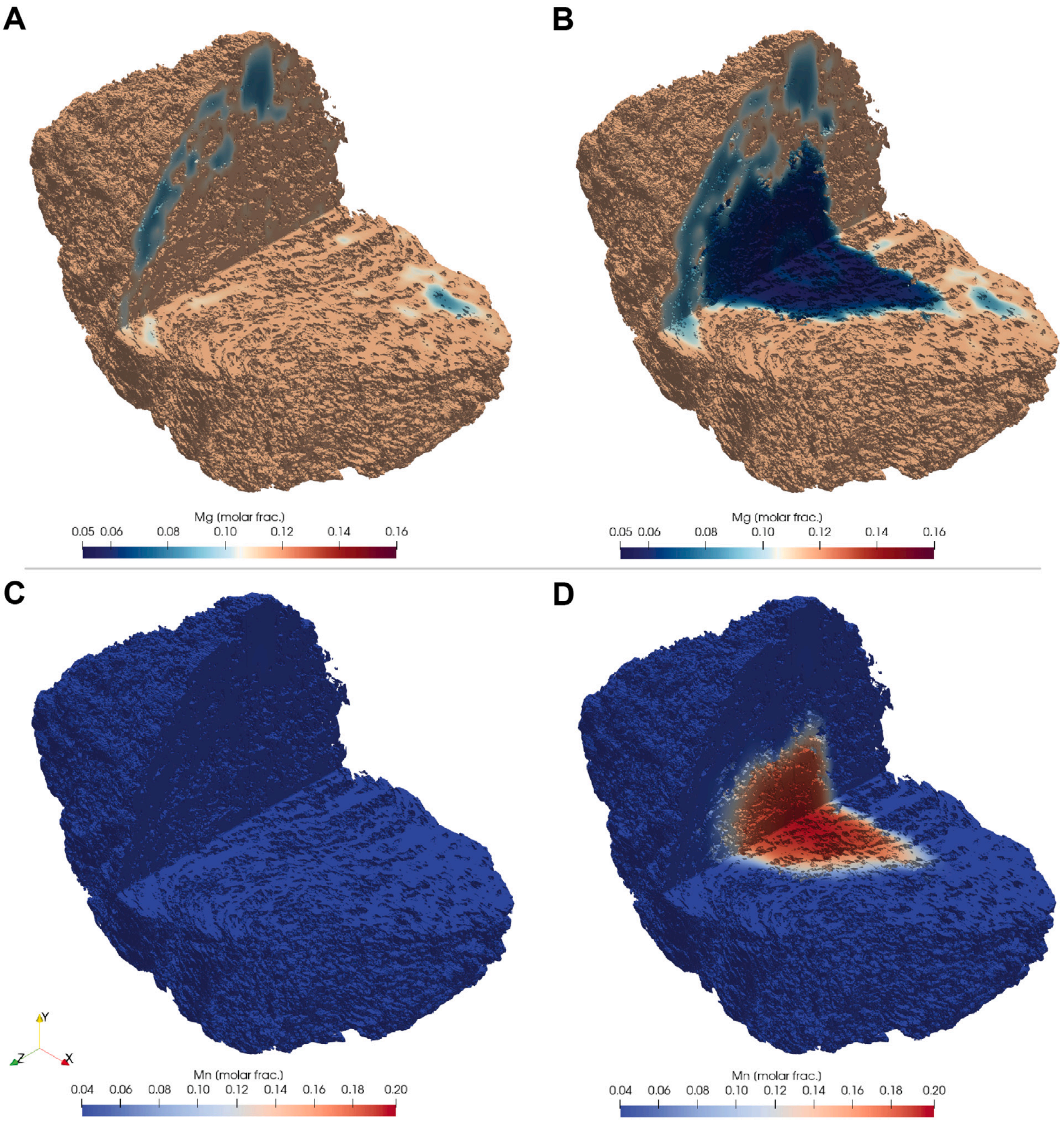

Fig. 8. Final timestep after 10 Myr for Mg (top) in (A) the open garnet model (OGM) and (B) the isolated matrix model (IMM), and for Mn (bottom) in (C) OGM and (D) IMM. A quarter of the grain is removed for visualisation. Temperature and pressure remain constant at 700 °C and 0.8 GPa. The initial setups from the two models differ only by their boundary conditions: the composition in the garnet is fixed to $\overline{C^{eq}}$ in contact with all the matrix ($\partial\Omega^{M}_{\mathrm{Grt}}$) in DMG. In contrast, in IMM, the garnet does not exchange chemically with the matrix near the core. The resolution is 768^3 for both models.

from 2 to 2.5 mm). Uphill diffusion is a phenomenon predicted in multicomponent diffusion systems, when an element diffuses against its composition gradient (Onsager, 1945; Darken, 1948; Ganguly, 2010). Mathematically, uphill diffusion for an element x is more likely to occur when the values of its off-diagonal terms in the interdiffusion coefficient matrix ($D_{i=x,j\neq x}$) are in the same or higher order of magnitude compared to its diagonal term ($D_{i=x,j=x}$). This is likely the case for the D_{FeMn} term in both OGM and IMM, given the rapid decrease in Mn, which is influenced by the enforced boundary condition at the matrix-garnet interface. This is supported by the strong correlation between the observed uphill diffusion of Fe and the corresponding reduction in Mn content (Fig. 13B and C). While uphill diffusion has been observed both numerically and experimentally in garnet (Vielzeuf and Saúl, 2011; Ganguly, 2002), there has been no conclusive evidence of uphill diffusion in natural garnet samples, with only few potential candidates (e.g. Carlson, 2006; Raimbourg et al., 2007). This arises from two key challenges: distinguishing between growth zoning and diffusion in natural samples, and reconstructing the initial conditions in a diffusion-dominated system, where multiple different initial states can evolve into the same final composition due to the multicomponent nature of the diffusion. This means that if present, the results of uphill diffusion are hard to assess with certainty. The numerical

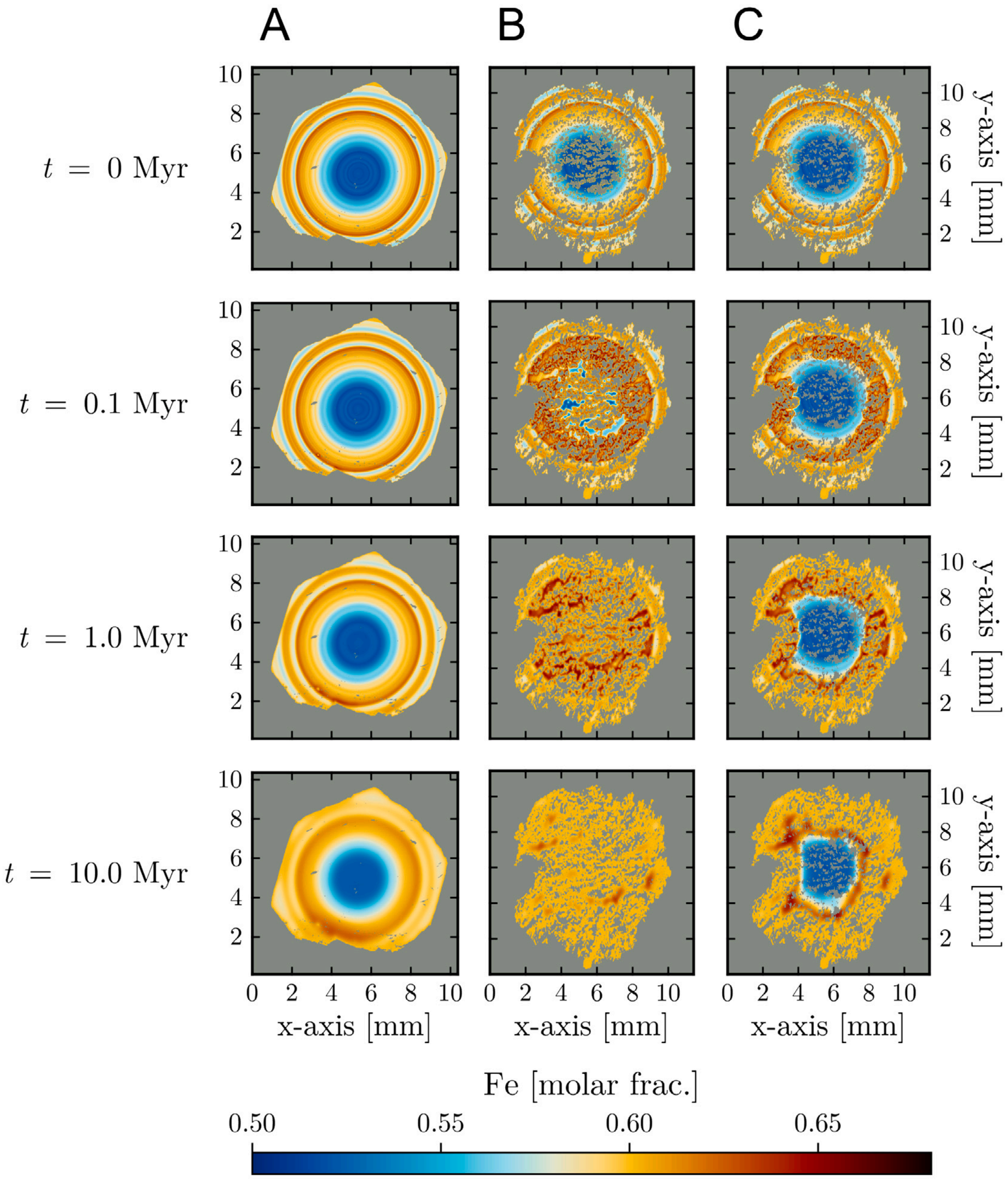

Fig. 9. Evolution through time in 2D of the Fe composition of the three models: (A) euhedral garnet model (EGM), (B) open garnet model (OGM), and (C) isolated matrix model (IMM). The 2D section is a central section normal to the z-axis. Pressure and temperature are constant and fixed to 0.8 GPa and 700 °C. The total resolution of all models is 768^3.

models predict that uphill diffusion may be common for complex garnet geometries when the initial Mn content is high, due to local equilibrium at the interface with the surrounding matrix and the high diffusivity of this element in garnet.

4.4. Assumptions, implications, and limitations

The definitions of the boundaries in the models are key assumptions. By fixing the composition of the garnet in contact with the matrix, grain boundary equilibrium is assumed. This implies that elemental exchange between the garnet and surrounding phases occurs faster than intra-grain diffusion timescales, thus ensuring equilibrium. Whether this assumption accurately reflects natural metamorphic systems remains an open question (e.g. Carlson et al., 2015; Lanari and Engi, 2017; Dempster et al., 2017). If valid, it suggests that matrix interactions with the inner part of garnet grains, as demonstrated by OGM, could provide an efficient mechanism for replenishing the matrix with elements such as Mn. This exchange of elements between intra- and inter-granular domains could facilitate the growth of new mineral phases. Similar core-matrix interactions have been previously documented on natural samples (Konrad-Schmolke et al., 2007). Furthermore, in garnet, complex asymmetrical compositional zonations that deviate from simple concentric zoning is a relatively common occurrence in the rock record. This has often be linked to diffusion occurring around inclusions or because of fast diffusion pathways linked to the matrix (e.g. Lanari and Hermann, 2021; Smit et al., 2013; Keller, 2006), supporting what the models predict. However, the extent to which such exchange occurs remains to be fully assessed, with significant implications for

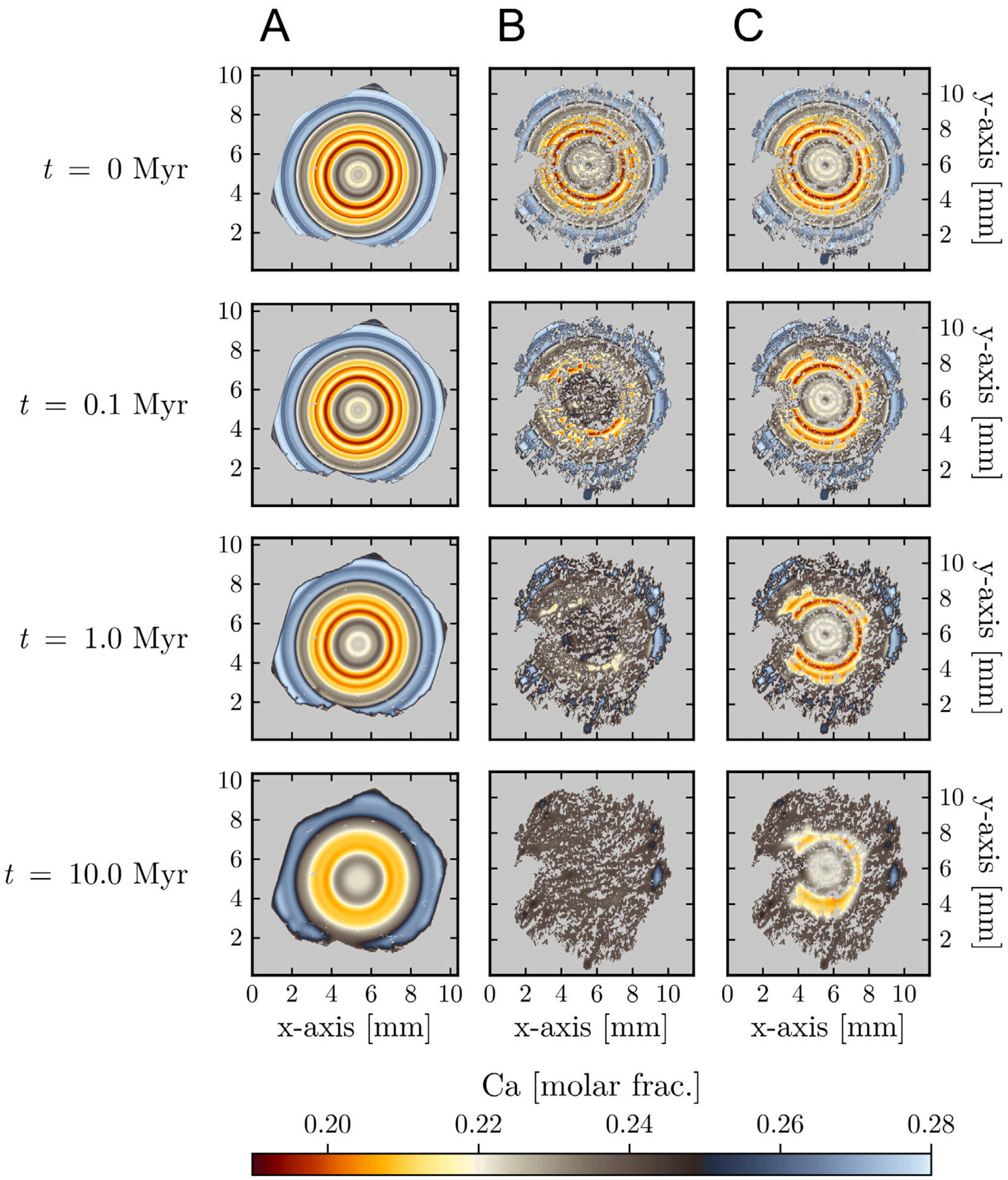

Fig. 10. Evolution through time in 2D of the Ca composition of the three models: (A) euhedral garnet model (EGM), (B) open garnet model (OGM), and (C) isolated matrix model (IMM). The 2D section is a central section normal to the *z*-axis. Pressure and temperature are constant and fixed to 0.8 GPa and 700 °C. The total resolution of all models is 768^3.

the preservation of original zoning and chemical re-equilibration, as highlighted by IMM. Finally, in more realistic scenarios, *P*–*T* conditions could change within the modelling timescale. Apart from impacting the diffusion processes themselves, an important consequence of this would be a change in the composition of the garnet in equilibrium with the matrix, as shown by previous studies modelling syn-growth diffusion (Caddick et al., 2010; Florence and Spear, 1991; Gaidies et al., 2008; Faryad and Ježek, 2019).

The role of inclusions, represented by Ω_I, has been deliberately simplified by applying a no-flux boundary on $\partial\Omega^I_{\mathrm{Grt}}$ and treating all inclusions as part of a single domain. Many common inclusions in garnet, such as quartz, rutile, muscovite, zircon, and aluminosilicates, are not involved in major element diffusion due to their structural composition. However, other inclusions, such as biotite, ilmenite, or amphibole, can exchange chemically with garnet, and their partitioning behaviour has been used to estimate cooling rates (Ferry and Spear, 1978; Spear and Parrish, 1996; Pownceby et al., 1987; Bento Dos Santos et al., 2014). While this study does not consider the complexity of multiple inclusion types within a single garnet grain, the numerical framework presented here could be extended in future work to investigate their role in garnet diffusion. By defining distinct domains for each inclusion type with appropriate boundary conditions, this could provide new insights into the role of inclusions in garnet diffusion in 3D.

Another simplification in this study is the assumption that the initial garnet composition follows an ellipsoidal distribution. Whilst

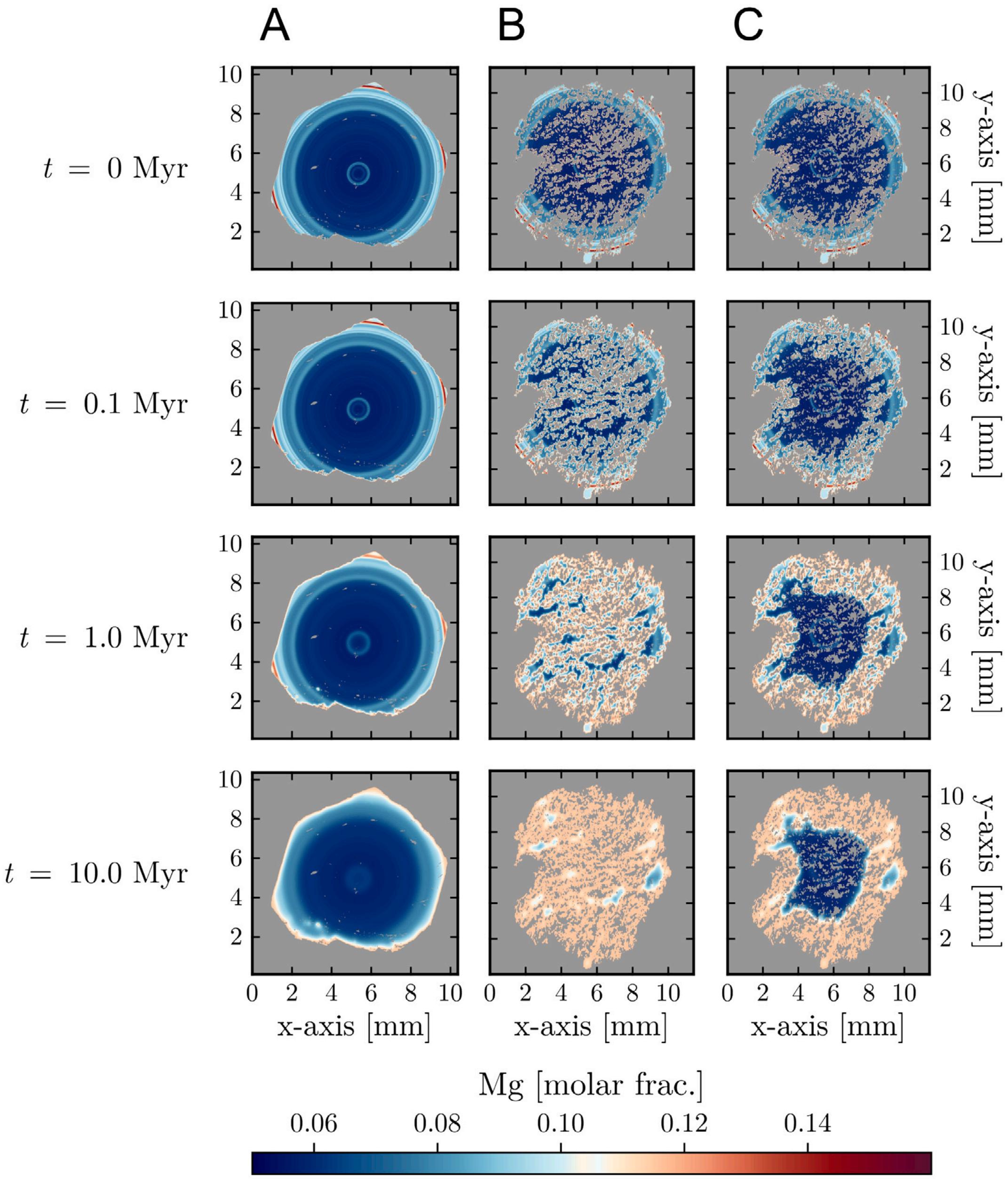

Fig. 11. Evolution through time in 2D of the Mg composition of the three models: (A) euhedral garnet model (EGM), (B) open garnet model (OGM), and (C) isolated matrix model (IMM). The 2D section is a central section normal to the *z*-axis. Pressure and temperature are constant and fixed to 0.8 GPa and 700 °C. The total resolution of all models is 768^3.

this is reasonable for euhedral to sub-euhedral grains, more complex grain geometries, resulting for example from significant syn- to post-growth deformation or resorption, would require alternative approaches. Extracting composition, at least quantitatively, from µCT imaging or others 3D imaging techniques would greatly improve this shortcoming. This would allow the exploration of more complex scenarios and further improve our understanding of the interplay between intra- and intergranular diffusion processes.

Finally, while the current models are based on geologically sound assumptions, they lack a systematic exploration of parameter space and the incorporation of data-driven constraints. Future developments could employ sensitivity analysis to more accurately quantify the influence of boundary conditions or use inverse modelling approaches to optimise model parameters to fit observed compositional data. However, this would require suitable natural samples with well-established constraints, such as *P*–*T*–*t* paths and initial conditions. This would formalise the link between model predictions and observations, enabling more robust interpretations of natural garnet zoning and its implications for metamorphic processes.

5. Conclusion

This study presents a framework for simulating major element diffusion in garnet using realistic 3D grain geometries derived from

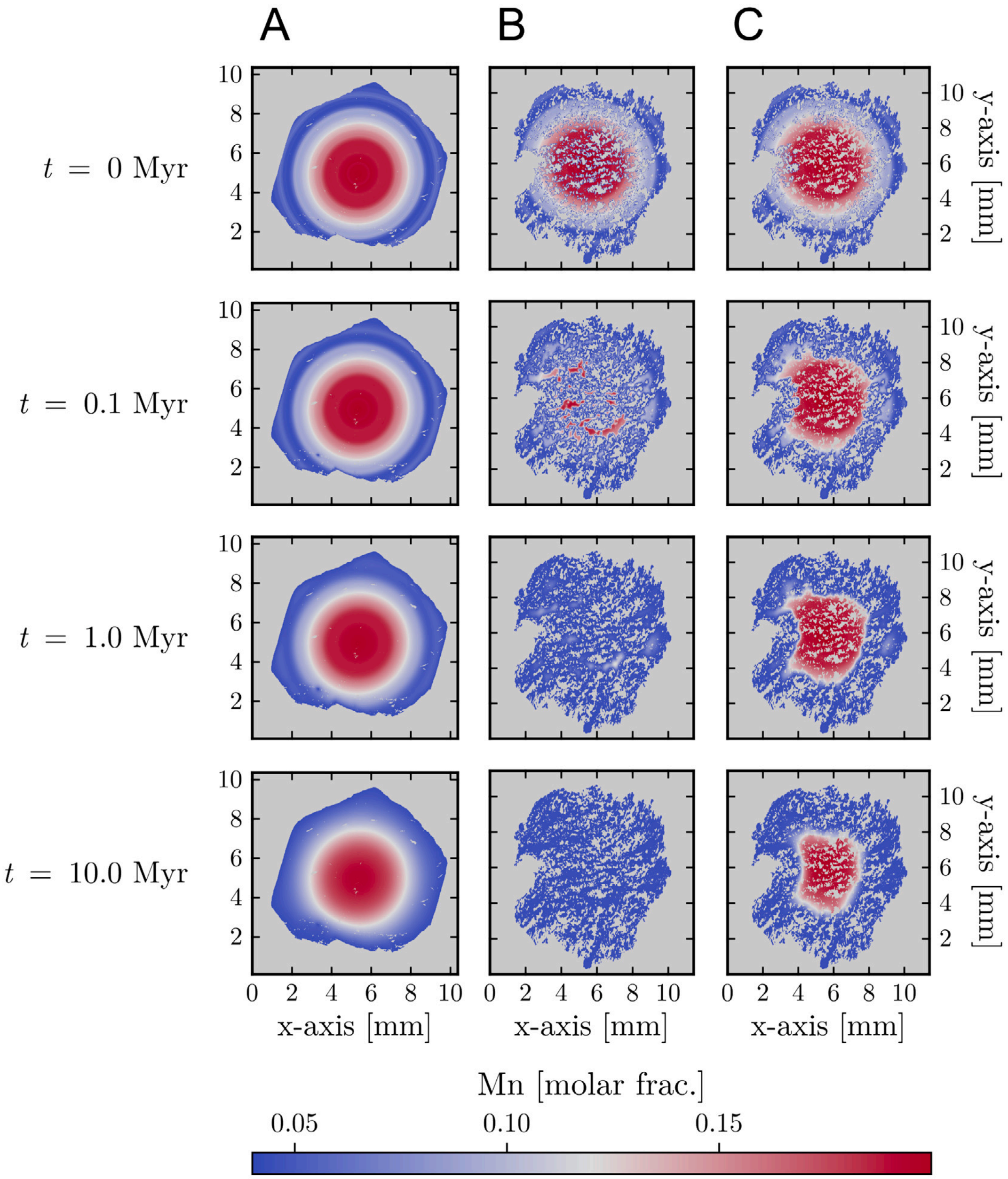

Fig. 12. Evolution through time in 2D of the Mn composition of the three models: (A) euhedral garnet model (EGM), (B) open garnet model (OGM), and (C) isolated matrix model (IMM). The 2D section is a central section normal to the z-axis. Pressure and temperature are constant and fixed to 0.8 GPa and 700 °C. The total resolution of all models is 768^3.

μCT data. Using a high performance numerical solver with GPU acceleration from the DiffusionGarnet.jl package, we have demonstrated the efficiency of stabilised explicit methods, in particular the ROCK2 solver (Abdulle and Medovikov, 2001), in solving multicomponent diffusion equations at high resolution. As stabilised explicit methods are suitable for solving large middly-stiff diffusion-dominated parabolic PDEs, ROCK2 shows potential to be used for other systems described by this kind of equations in Geosciences, such as thermal or erosion modelling in 2D or 3D to gain performance and scalability. Furthermore, as those methods are time-stepping methods, they can also be used with other popular spatial discretisation methods, such as finite element.

Comparison of different garnet morphologies highlights the critical role of grain geometry and matrix connectivity in controlling diffusion rates and zoning preservation. Our results confirm that diffusion in euhedral garnets closely follows predictions based on spherical assumptions, whereas sub-euhedral garnets with high connectivity to the matrix undergo significant compositional re-equilibration. In particular, the isolated matrix model also shows that the ability for garnet to reach local equilibrium with the surrounding matrix controls the preservation or not of the original zoning. Better constraints on inter-granular diffusion are therefore important to accurately model this process.

These results highlight the importance of considering realistic 3D geometries in diffusion studies and support the idea that complex grains can only be properly modelled by taking into account all dimensions, as connectivity from the matrix, which is critical for diffusion, is impossible to assess from a simple 2D cross-section. Future applications of this framework could include the incorporation of additional petrological complexities, such as garnet growth, variable matrix composition,

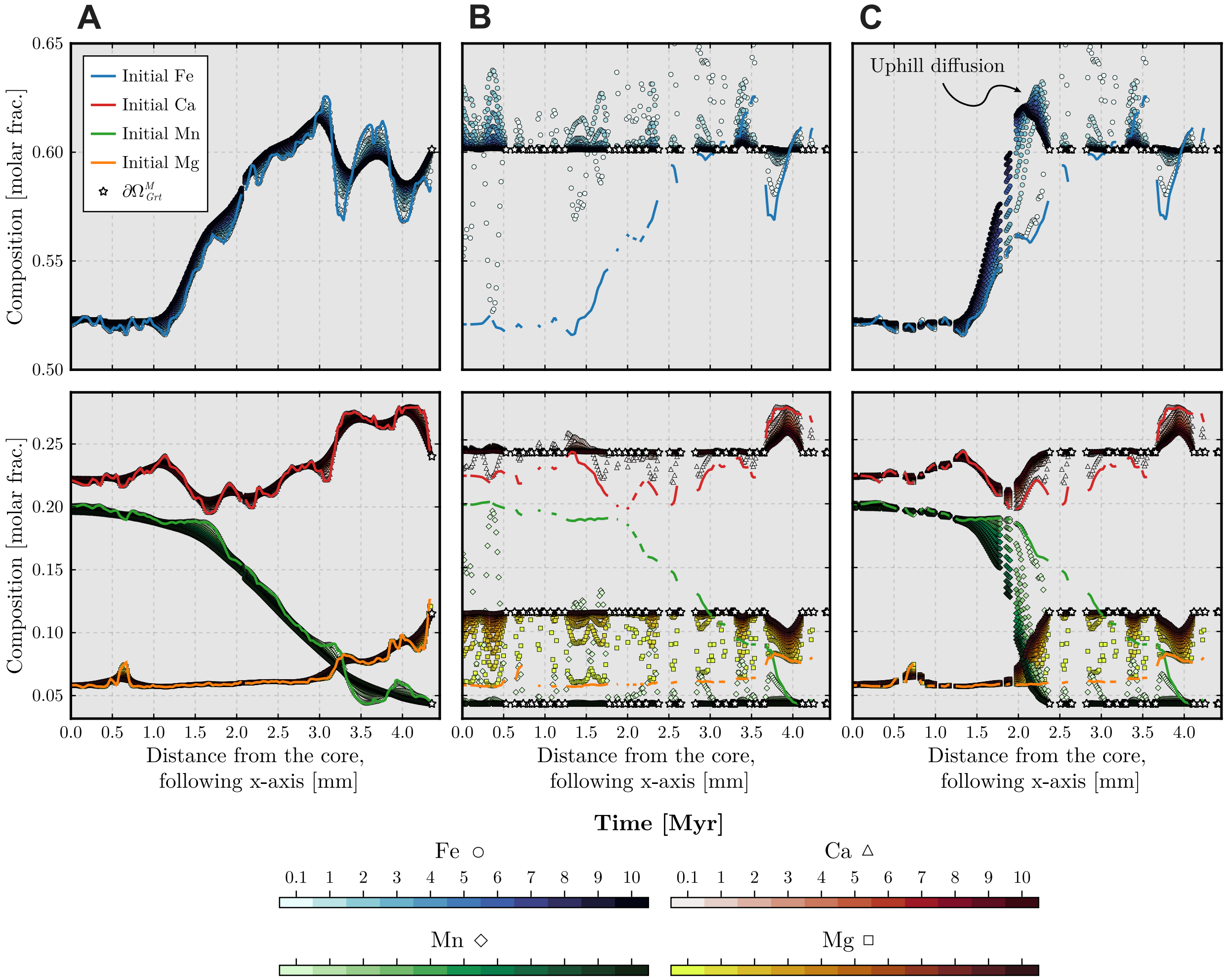

Fig. 13. Time evolution of composition during 10 Myr along a 1D core-rim profile following the x-axis for (A) the euhedral garnet model (EGM), (B) the open garnet model (OGM), and (C) the isolated matrix model (IMM). Temperature and pressure remain constant at 700 °C and 0.8 GPa. The white stars represent the position where a Dirichlet boundary condition is enforced. The initial setups for (B) and (C) differ only by their boundary conditions: the composition in the garnet is fixed to $\overline{C^{\mathrm{eq}}}$ in contact with all the matrix ($\partial\Omega^{M}_{\mathrm{Grt}}$) in DMG. In contrast, in IMM, the garnet does not exchange chemical element with the matrix near the core. The total resolution of the three 3D models is 768^3.

complex P–T–t paths and the role of inclusions exchanging chemically with garnet.

CRediT authorship contribution statement

Hugo Dominguez: Writing – review & editing, Writing – original draft, Visualization, Validation, Supervision, Software, Methodology, Investigation, Formal analysis, Data curation, Conceptualization. **Nathan Mäder:** Writing – review & editing, Software, Methodology, Investigation, Formal analysis. **Pierre Lanari:** Writing – review & editing, Validation, Supervision, Resources, Project administration, Funding acquisition, Conceptualization.

Code availability

The source code is available for downloading on Github (https://github.com/Iddingsite/DiffusionGarnet.jl) and at a permanent DOI repository (Zenodo): https://zenodo.org/records/15046913 (Dominguez, 2025a). The code is written in the Julia programming language and is distributed under the GPL-3.0 license. The version used of DiffusionGarnet.jl for this article is 0.2.4. The Julia version is 1.11.2. The scripts used for running the specific models of this manuscript are also present in a separate repository on Github (https://github.com/Iddingsite/DiffusionGarnet_3D.jl) and at a permanent DOI repository (Zenodo): https://zenodo.org/records/15680919 (Dominguez, 2025b).

Declaration of competing interest

The authors declare that they have no known competing financial interests or personal relationships that could have appeared to influence the work reported in this paper.

Acknowledgements

HD thanks Ivan Utkin for help with non-dimensionalisation, Ludovic Räss for the introduction to ParallelStencil.jl and discussions, and Pascal Aellig for support in running the models on the Grace Hopper superchip in the Johannes Gutenberg University, Mainz. Bernardo Cesare is acknowledged for providing the original sample from which the chemical profile was extracted. The authors are grateful to two anonymous reviewers for their thorough and constructive reviews of the original draft, and Pauline Collon for her editorial handling. Funding was provided by the European Research Council (ERC) under the European Union's Horizon 2020 research and innovation programme (grant agreement No 850530). HD acknowledges funding by the Institute of Multiscale Modelling (M3ODEL) from the Johannes Gutenberg University in Mainz, Germany.

Appendix A. Supplementary data

Supplementary material related to this article can be found online at https://doi.org/10.1016/j.cageo.2025.106023.

Data availability

The initial conditions of each model at different resolutions are stored in a separate Zenodo repository: https://zenodo.org/records/15045718 (Dominguez, 2025c). The results of the models are available on request.

References

Abdulle, A., 2002. Fourth order Chebyshev methods with recurrence relation. SIAM J. Sci. Comput. 23 (6), 2041–2054. http://dx.doi.org/10.1137/S1064827500379549.

Abdulle, A., 2015. Explicit stabilized runge–kutta methods. In: Engquist, Björn (Ed.), Encyclopedia of Applied and Computational Mathematics. Springer, pp. 460–468. http://dx.doi.org/10.1007/978-3-540-70529-1_100.

Abdulle, A., Grote, M., Rosilho De Souza, G., 2022. Explicit stabilized multirate method for stiff differential equations. Math. Comp. http://dx.doi.org/10.1090/mcom/3753.

Abdulle, A., Medovikov, A.A., 2001. Second order Chebyshev methods based on orthogonal polynomials. Numer. Math. 90 (1), 1–18. http://dx.doi.org/10.1007/s002110100292.

Ague, J.J., Baxter, E.F., 2007. Brief thermal pulses during mountain building recorded by Sr diffusion in apatite and multicomponent diffusion in garnet. Earth Planet. Sci. Lett. 261 (3–4), 500–516. http://dx.doi.org/10.1016/j.epsl.2007.07.017.

Ague, J.J., Carlson, W.D., 2013. Metamorphism as garnet sees it: The Kinetics of nucleation and growth, equilibration, and diffusional relaxation. Elements 9 (6), 439–445. http://dx.doi.org/10.2113/gselements.9.6.439.

Ahrens, J., Geveci, B., Law, C., Hansen, C., Johnson, C., et al., 2005. 36-Paraview: an end-user tool for large-data visualization. Vis. Handb. 717, 50038–1.

Atherton, M.P., Edmunds, W.M., 1966. An electron microprobe study of some zoned garnets from metamorphic rocks. Earth Planet. Sci. Lett. 1 (4), 185–193.

Baxter, E.F., Caddick, M.J., Ague, J.J., 2013. Garnet: common mineral, uncommonly useful. Elements 9 (6), 415–419. http://dx.doi.org/10.2113/gselements.9.6.415.

Baxter, E.F., Caddick, M.J., Dragovic, B., 2017. Garnet: A rock-forming mineral petrochronometer. Rev. Miner. Geochem. 83 (1), 469–533. http://dx.doi.org/10.2138/rmg.2017.83.15.

Bento Dos Santos, T.M., Tassinari, C.C.G., Fonseca, P.E., 2014. Garnet-Biotite diffusion mechanisms in complex high-grade orogenic belts: understanding and constraining petrological cooling rates in granulites from ribeira fold belt (SE Brazil). J. South Am. Earth Sci. 56, 128–138. http://dx.doi.org/10.1016/j.jsames.2014.09.003.

Besard, T., Foket, C., De Sutter, B., 2018. Effective extensible programming: unleashing julia on GPUs. IEEE Trans. Parallel Distrib. Syst. http://dx.doi.org/10.1109/TPDS.2018.2872064.

Bezanson, J., Edelman, A., Karpinski, S., Shah, V.B., 2017. Julia: A fresh approach to numerical computing. SIAM Rev. 59 (1), 65–98. http://dx.doi.org/10.1137/141000671.

Caddick, M.J., Konopásek, J., Thompson, A.B., 2010. Preservation of garnet growth zoning and the duration of prograde metamorphism. J. Petrol. 51 (11), 2327–2347. http://dx.doi.org/10.1093/petrology/egq059.

Carlson, W.D., 2002. Scales of disequilibrium and rates of equilibration during metamorphism. Am. Mineral. 87 (2–3), 185–204. http://dx.doi.org/10.2138/am-2002-2-301.

Carlson, W.D., 2006. Rates of Fe, Mg, Mn, and Ca diffusion in garnet. Am. Mineral. 91 (1), 1–11. http://dx.doi.org/10.2138/am.2006.2043.

Carlson, W.D., Pattison, D.R.M., Caddick, M.J., 2015. Beyond the equilibrium paradigm: How consideration of kinetics enhances metamorphic interpretation. Am. Mineral. 100 (8–9), 1659–1667. http://dx.doi.org/10.2138/am-2015-5097.

Cesare, B., Nestola, F., Johnson, T., Mugnaioli, E., Della Ventura, G., Peruzzo, L., Bartoli, O., Viti, C., Erickson, T., 2019. Garnet, the archetypal cubic mineral, grows tetragonal. Sci. Rep. 9 (1), 14672. http://dx.doi.org/10.1038/s41598-019-51214-9.

Chakraborty, S., Ganguly, J., 1992. Cation diffusion in aluminosilicate garnets: Experimental determination in spessartine-almandine diffusion couples, evaluation of effective binary diffusion coefficients, and applications. Contrib. Miner. Pet. 111 (1), 74–86. http://dx.doi.org/10.1007/BF00296579.

Cheng, H., Bloch, E.M., M., Evangelos, Vervoort, J.D., 2020. Reconciliation of discrepant U–Pb, Lu–Hf, Sm–Nd, Ar–Ar and U–Th/He dates in an amphibolite from the cathaysia block in Southern China. Contrib. Miner. Pet. 175 (1), 4. http://dx.doi.org/10.1007/s00410-019-1644-9.

Courant, R., Friedrichs, K., Lewy, H., 1928. Über die partiellen Differenzengleichungen der mathematischen Physik. Math. Ann. 100 (1), 32–74.

Danisch, S., Krumbiegel, J., 2021. Makie.jl: flexible high-performance data visualization for julia. J. Open Source Softw. 6 (65), 3349. http://dx.doi.org/10.21105/joss.03349.

Darken, L.S., 1948. Diffusion, mobility and their interrelation through free energy in binary metallic systems. Trans. Aime 175, 184–201.

Dempster, T.J., 1985. Garnet zoning and metamorphism of the barrovian type area, Scotland. Contrib. Miner. Pet. 89 (1), 30–38. http://dx.doi.org/10.1007/BF01177588.

Dempster, T.J., Symon, S., Chung, P., 2017. Intergranular diffusion rates from the analysis of garnet surfaces: implications for metamorphic equilibration. J. Metamorph. Geol. 35 (6), 585–600. http://dx.doi.org/10.1111/jmg.12247.

Devoir, A., Bloch, E., Müntener, O., 2021. Residence time of igneous garnet in Si-rich magmatic systems: Insights from diffusion modeling of major and trace elements. Earth Planet. Sci. Lett. 560, 116771. http://dx.doi.org/10.1016/j.epsl.2021.116771.

Dominguez, H., 2023. DiffusionGarnet.jl. URL: https://doi.org/10.5281/zenodo.10425700.

Dominguez, H., 2025a. Iddingsite/DiffusionGarnet.jl: V0.2.4. http://dx.doi.org/10.5281/zenodo.15046913.

Dominguez, H., 2025b. Iddingsite/DiffusionGarnet_3D.jl: V0.1.1. http://dx.doi.org/10.5281/zenodo.15680919.

Dominguez, H., 2025c. Initial conditions for the models of the manuscript "simulating major element diffusion in garnet using realistic 3D geometries" from dominguez et al. 2025. http://dx.doi.org/10.5281/zenodo.15045718.

Dumont, T., Duarte, M., Descombes, S., Dronne, M., Massot, M., Louvet, V., 2013. Simulation of human ischemic stroke in realistic 3D geometry. Commun. Nonlinear Sci. Numer. Simul. 18 (6), 1539–1557. http://dx.doi.org/10.1016/j.cnsns.2012.10.002.

Evans, B.W., 1965. Microprobe study of zoning in eclogite garnets. Abstr Geol Soc Am Spec Pap 87, 54.

Faryad, S.W., Chakraborty, S., 2005. Duration of Eo-Alpine metamorphic events obtained from multicomponent diffusion modeling of garnet: A case study from the Eastern Alps. Contrib. Miner. Pet. 150 (3), 306–318. http://dx.doi.org/10.1007/s00410-005-0020-0.

Faryad, S.W., Ježek, J., 2019. Compositional zoning in garnet and its modification by diffusion during pressure and temperature changes in metamorphic rocks; an approach and software. Lithos 332–333, 287–295. http://dx.doi.org/10.1016/j.lithos.2019.03.002.

Ferry, J.M., Spear, F.S., 1978. Experimental calibration of the partitioning of fe and mg between Biotite and garnet. Contrib. Miner. Pet. 66 (2), 113–117. http://dx.doi.org/10.1007/BF00372150.

Fick, A., 1855. On liquid diffusion. Lond. Edinb. Dublin Philos. Mag. J. Sci. 10 (63), 30–39. http://dx.doi.org/10.1080/14786445508641925.

Florence, F.P., Spear, F.S., 1991. Effects of diffusional modification of garnet growth zoning on p-t path calculations. Contrib. Miner. Pet. 107 (4), 487–500. http://dx.doi.org/10.1007/BF00310683.

Gaidies, F., de Capitani, C., Abart, R., 2008. THERIA_G: A software program to numerically model prograde garnet growth. Contrib. Miner. Pet. 155 (5), 657–671. http://dx.doi.org/10.1007/s00410-007-0263-z.

Gaidies, F., Heldwein, O.K.A., Yogi, M.T.A.G., Cutts, J.A., Smit, M.A., Rice, A.H.N., 2022. Testing the equilibrium model: An example from the caledonian kalak nappe complex (finnmark, arctic Norway). J. Metamorph. Geol. 40 (5), 859–886. http://dx.doi.org/10.1111/jmg.12648.

Ganguly, J., 2002. Diffusion kinetics in minerals: Principles and applications to tectono-metamorphic processes. In: Gramaccioli, Carlo Maria, Papp, Gábor, Weiszburg, Tamás (Eds.), Energy Modelling in Minerals. Mineralogical Society of Great Britain and Ireland, pp. 271–309. http://dx.doi.org/10.1180/EMU-notes.4.9.

Ganguly, J., 2010. Cation diffusion kinetics in aluminosilicate garnets and geological applications. Rev. Miner. Geochem. 72 (1), 559–601. http://dx.doi.org/10.2138/rmg.2010.72.12.

Ganguly, J., Chakraborty, S., Sharp, T.G., Rumble, D., 1996. Constraint on the time scale of Biotite-grade metamorphism during acadian orogeny from a natural garnet-garnet diffusion couple. Am. Mineral. 81 (9–10), 1208–1216. http://dx.doi.org/10.2138/am-1996-9-1019.

Ganguly, J., Dasgupta, S., Cheng, W., Neogi, S., 2000. Exhumation history of a section of the Sikkim Himalayas, India: Records in the metamorphic mineral equilibria and compositional zoning of garnet. Earth Planet. Sci. Lett. 183 (3–4), 471–486. http://dx.doi.org/10.1016/S0012-821X(00)00280-6.

Gendron, M., Fontaine, J., Provencher, B., Yen, E., Piché, N., Marsh, M., 2021. Centralizing digital resources for data management, processing, and analysis for enterprise scale imaging research. Microsc. Microanal. 27 (S1), 1084–1085. http://dx.doi.org/10.1017/S1431927621004086.

George, F.R., Gaidies, F., 2017. Characterisation of a garnet population from the Sikkim Himalaya: Insights into the rates and mechanisms of porphyroblast crystallisation. Contrib. Miner. Pet. 172 (7), 57. http://dx.doi.org/10.1007/s00410-017-1372-y.

Hairer, E., Wanner, G., 1996. Solving ordinary differential equations II. In: Springer Series in Computational Mathematics, vol. 14, Springer Berlin Heidelberg, http://dx.doi.org/10.1007/978-3-642-05221-7.

Hairer, E., Wanner, G., Nørsett, S.P., 1993. Solving ordinary differential equations i. In: Springer Series in Computational Mathematics, vol. 8, Springer, http://dx.doi.org/10.1007/978-3-540-78862-1.

Hand, L.N., Finch, J.D., 1998. Analytical Mechanics. Cambridge University Press.

Hartmeier, P., Lanari, P., Forshaw, J.B., Markmann, T.A., 2024. Tracking garnet dissolution kinetics in 3D using deep learning grain shape classification. J. Petrol. 65 (3), egae005. http://dx.doi.org/10.1093/petrology/egae005.

Hollister, L.S., 1966. Garnet zoning: An interpretation based on the Rayleigh fractionation model. Sci. 154 (3757), 1647–1651. http://dx.doi.org/10.1126/science.154.3757.1647.

Kaus, B., de Montserrat, A., Medinger, N., Aellig, P., Dominguez, H., Riel, N., Cosarinsky, M., Berlie, N., Spang, A., dkiss-THMC, Ranocha, H., Fuchs, L., Frasunkiewicz, J., Räss, L., Seiler, A., Duretz, T., 2025. JuliaGeodynamics/GeoParams.Jl: V0.7.0. http://dx.doi.org/10.5281/zenodo.14772896.

Keller, L.M., 2006. Enhanced mass transfer through short-circuit diffusion: growth of garnet reaction rims at eclogite facies conditions. Am. Mineral. 91 (7), 1024–1038. http://dx.doi.org/10.2138/am.2006.2068.

Keller, A., Contributors, 2025. PainterQubits/Unitful.Jl: physical quantities with arbitrary units. URL: https://github.com/PainterQubits/Unitful.jl.

Ketcham, R.A., Carlson, W.D., 2001. Acquisition, optimization and interpretation of X-ray computed tomographic imagery: Applications to the geosciences. Comput. Geosci. 27 (4), 381–400.

Kleefeld, B., Martín-Vaquero, J., 2013. SERK2v2: A new second-order stabilized explicit runge-kutta method for stiff problems. Numer. Methods Partial Differential Equations 29 (1), 170–185.

Konrad-Schmolke, Ma., O Brien, P.J., Heidelbach, F., 2007. Compositional re-equilibration of garnet: The importance of sub-grain boundaries. Eur. J. Mineral. 19 (4), 431–438. http://dx.doi.org/10.1127/0935-1221/2007/0019-1749.

Lanari, P., Engi, M., 2017. Local bulk composition effects on metamorphic mineral assemblages. Rev. Miner. Geochem. 83 (1), 55–102. http://dx.doi.org/10.2138/rmg.2017.83.3.

Lanari, P., Giuntoli, F., Loury, C., Burn, M., Engi, M., 2017. An inverse modeling approach to obtain P–T conditions of metamorphic stages involving garnet growth and resorption. Eur. J. Mineral. 29 (2), 181–199. http://dx.doi.org/10.1127/ejm/2017/0029-2597.

Lanari, P., Hermann, J., 2021. Iterative thermodynamic modelling—part 2: tracing equilibrium relationships between minerals in metamorphic rocks. J. Metamorph. Geol. 39 (6), 651–674. http://dx.doi.org/10.1111/jmg.12575.

Lanari, P., Tedeschi, M., 2025. Chemical map classification in xMapTools. Appl. Comput. Geosci. 25, 100230. http://dx.doi.org/10.1016/j.acags.2025.100230.

Lanari, P., Vho, A., Bovay, T., Airaghi, L., Centrella, S., 2019. Quantitative compositional mapping of mineral phases by electron probe micro-analyser. Geol. Soc. Lond. Spec. Publ. 478 (1), 39–63.

Lanari, P., Vidal, O., De Andrade, V., Dubacq, B., Lewin, E., Grosch, E.G., Schwartz, S., 2014. XMapTools: a MATLAB ©-based program for electron microprobe X-ray image processing and geothermobarometry. Comput. Geosci. 62, 227–240. http://dx.doi.org/10.1016/j.cageo.2013.08.010.

Lasaga, A.C., 1979. Multicomponent exchange and diffusion in silicates. Geochim. Cosmochim. Acta 43 (4), 455–469. http://dx.doi.org/10.1016/0016-7037(79)90158-3.

Lasaga, A.C., 1983. Geospeedometry: An extension of geothermometry. In: Kinetics and Equilibrium in Mineral Reactions. Springer, pp. 81–114.

Li, Z.M.G., Gaidies, F., Chen, Y.C., Zhao, Y.L., Wu, C.M., 2024. Petrogenesis of sector-zoned garnet in graphitic metapelite from the danba dome, eastern tibetan plateau (SW China). Contrib. Miner. Pet. 179 (6), 56. http://dx.doi.org/10.1007/s00410-024-02139-8.

Li, B., Ge, J., Zhang, B., 2018. Diffusion in garnet: A review. Acta Geochim. 37 (1), 19–31. http://dx.doi.org/10.1007/s11631-017-0187-x.

Loomis, T.P., Ganguly, J., Elphick, S.C., 1985. Experimental determination of cation diffusivities in aluminosilicate garnets: II. multicomponent simulation and tracer diffusion coefficients. Contrib. Miner. Pet. 90, 45–51.

Manzotti, P., Regis, D., Petts, D.C., Graziani, R., Polivchuk, M., 2024. Formation of multistage garnet grains by fragmentation and overgrowth constrained by microchemical and microstructural mapping. J. Metamorph. Geol. 42 (4), 471–496. http://dx.doi.org/10.1111/jmg.12761.

Martín-Vaquero, J., Kleefeld, A., 2019. ESERK5: A fifth-order extrapolated stabilized explicit runge–kutta method. J. Comput. Appl. Math. 356, 22–36. http://dx.doi.org/10.1016/j.cam.2019.01.040.

Mutch, E.J.F., Maclennan, J., Shorttle, O., Rudge, J.F., Neave, D.A., 2021. DFENS: diffusion chronometry using finite elements and nested sampling. Geochem. Geophys. Geosystems 22 (4), e2020GC009303. http://dx.doi.org/10.1029/2020GC009303.

Newman, W.M., Sproull, R.F., 1979. Principles of Interactive Computer Graphics. McGraw-Hill, Inc..

Omlin, S., Räss, L., 2022. High-performance xPU stencil computations in julia. http://dx.doi.org/10.48550/arXiv.2211.15634, URL: http://arxiv.org/abs/2211.15634 (visited 03 March 2025). Pre-published.

Onsager, L., 1931a. Reciprocal relations in irreversible processes. I.. Phys. Rev. 37 (4), 405–426. http://dx.doi.org/10.1103/PhysRev.37.405.

Onsager, L., 1931b. Reciprocal relations in irreversible processes. II.. Phys. Rev. 38 (12), 2265–2279. http://dx.doi.org/10.1103/PhysRev.38.2265.

Onsager, L., 1945. Theories and problems of liquid diffusion. Ann. New York Acad. Sci. 46 (5), 241–265. http://dx.doi.org/10.1111/j.1749-6632.1945.tb36170.x.

Pownceby, M.I., Wall, V.J., O'Neill, H.St.C., 1987. Fe-Mn partitioning between garnet and ilmenite: Experimental calibration and applications. Contrib. Miner. Pet. 97, 116–126.

Rackauckas, C., Nie, Q., 2017. DifferentialEquations.jl – a performant and feature-rich ecosystem for solving differential equations in julia. J. Open Res. Softw. 5 (1), 15. http://dx.doi.org/10.5334/jors.151.

Raimbourg, H., Goffé, B., Jolivet, L., 2007. Garnet reequilibration and growth in the eclogite facies and geodynamical evolution near peak metamorphic conditions. Contrib. Miner. Pet. 153 (1), 1–28. http://dx.doi.org/10.1007/s00410-006-0130-3.

Rubatto, D., Burger, M., Lanari, P., Hattendorf, B., Schwarz, G., Neff, C., Keresztes Schmidt, P., Hermann, J., Vho, A., Günther, D., 2020. Identification of growth mechanisms in metamorphic garnet by high-resolution trace element mapping with LA-ICP-TOFMS. Contrib. Miner. Pet. 175 (7), 61. http://dx.doi.org/10.1007/s00410-020-01700-5.

Schiesser, W.E., 2012. The Numerical Method of Lines: Integration of Partial Differential Equations. Elsevier Science.

Shea, T., Costa, F., Krimer, D., Hammer, J.E., 2015. Accuracy of timescales retrieved from diffusion modeling in olivine: a 3D perspective. Am. Mineral. 100 (10), 2026–2042. http://dx.doi.org/10.2138/am-2015-5163.

Smit, M.A., Scherer, E.E., Mezger, K., 2013. Peak metamorphic temperatures from cation diffusion zoning in garnet. J. Metamorph. Geol. 31 (3), 339–358. http://dx.doi.org/10.1111/jmg.12024.

Sommeijer, B.P., Shampine, L.F., Verwer, J.G., 1998. RKC: an explicit solver for parabolic PDEs. J. Comput. Appl. Math. 88 (2), 315–326. http://dx.doi.org/10.1016/S0377-0427(97)00219-7.

Spear, F.S., 2014. The duration of near-peak metamorphism from diffusion modelling of garnet zoning. J. Metamorph. Geol. 32 (8), 903–914. http://dx.doi.org/10.1111/jmg.12099.

Spear, F.S., Parrish, R.R., 1996. Petrology and cooling rates of the valhalla complex, British Columbia, Canada. J. Petrol. 37 (4), 733–765. http://dx.doi.org/10.1093/petrology/37.4.733.

Spear, F.S., Selverstone, J., Hickmott, D., Crowley, P., Hodges, K.V., 1984. P-t paths from garnet zoning: A new technique for deciphering tectonic processes in crystalline terranes. Geology 12 (2), 87–90. http://dx.doi.org/10.1130/0091-7613(1984)12<87:PPFGZA>2.0.CO;2.

Storey, C.D., Prior, D.J., 2005. Plastic deformation and recrystallization of garnet: A mechanism to facilitate diffusion creep. J. Petrol. 46 (12), 2593–2613. http://dx.doi.org/10.1093/petrology/egi067.

Tracy, R.J., Robinson, P., Thompson, A.B., 1976. Garnet composition and zoning in the determination of temperature and pressure of metamorphism, central massachusetts. Am. Mineral. 61 (7–8), 762–775.

Van Der Houwen, P.J., Sommeijer, B.P., 1980. On the internal stability of explicit, m-Stage Runge-Kutta Methods for large m-values. ZAMM - J. Appl. Math. Mech. / Z. Für Angew. Math. Und Mech. 60 (10), 479–485. http://dx.doi.org/10.1002/zamm.19800601005.

Vielzeuf, D., Saúl, A., 2011. Uphill diffusion, zero-flux planes and transient chemical solitary waves in garnet. Contrib. Miner. Pet. 161 (5), 683–702. http://dx.doi.org/10.1007/s00410-010-0557-4.

Woodsworth, G.J., 1977. Homogenization of zoned garnets from pelitic schists. Can. Miner. 15 (2), 230–242.

Wu, H., Zeng, L., Ge, R., Zhu, W., 2025. Finite element method for garnet diffusion chronometry. Geochem. Geophys. Geosystems 26 (4), e2025GC012182. http://dx.doi.org/10.1029/2025GC012182.

Yardley, B., 1977. An empirical study of diffusion in garnet. Am. Mineral. 62 (7–8), 793–800.